Specific and comprehensive genetic targeting reveals brain-wide distribution and synaptic input patterns of GABAergic axo-axonic interneurons

Ricardo Raudales[1,2,#], Gukhan Kim[1], Sean M. Kelly, [1,2,&], Joshua Hatfield[1,3], Wuqiang Guan[1], Shengli Zhao[3], Anirban Paul[1,5], Yongjun Qian[1,3], Bo Li[1], Z. Josh Huang [1,3,4]

[1]Cold Spring Harbor Laboratory, Cold Spring Harbor, NY 11724, USA
[2]Program in Neurobiology, Stony Brook University, NY, 11794, USA
[3]Department of Neurobiology, Duke University, Durham, NC 27710, USA
[4]Department of Biomedical Engineering, Duke University, Durham, NC 27710, USA
[5]Department of Neural and Behavioral Sciences, Penn State College of Medicine, Hershey, PA, 17033

current affiliations: [#]Department of Psychiatry, Columbia University, 1051 Riverside Drive, NY; Division of Molecular Therapeutics, New York State Psychiatric Institute, 1051 Riverside 11 Drive, NY. [&]Department of Neurology, NYU School of Medicine, New York, NY 10016

*Correspondence to: josh.huang@duke.edu

Abstract

Axo-axonic cells (AACs), also called chandelier cells (ChCs) in the cerebral cortex, are the most distinctive type of GABAergic interneurons described in the neocortex, hippocampus, and basolateral amygdala (BLA). AACs selectively innervate glutamatergic projection neurons (PNs) at their axon initial segment (AIS), thus may exert decisive control over PN spiking and regulate PN functional ensembles. However, the brain-wide distribution, synaptic connectivity, and circuit function of AACs remains poorly understood, largely due to the lack of specific and reliable experimental tools. Here, we have established an intersectional genetic strategy that achieves specific and comprehensive targeting of AACs throughout the mouse brain based on their lineage (*Nkx2.1*) and molecular (*Unc5b*, *Pthlh*) markers. We discovered that AACs are deployed across essentially all the pallium-derived brain structures, including not only the dorsal pallium-derived neocortex and medial pallium-derived hippocampal formation, but also the lateral pallium-derived claustrum-insular complex, and the ventral pallium-derived extended amygdaloid complex and olfactory centers. AACs are also abundant in anterior olfactory nucleus, taenia tecta and lateral septum. AACs show characteristic variations in density across neocortical areas and layers and across subregions of the hippocampal formation. Neocortical AACs comprise multiple laminar subtypes with distinct dendritic and axonal arborization patterns. Retrograde monosynaptic tracing from AACs across neocortical, hippocampal and BLA regions reveal shared as well as distinct patterns of synaptic input. Specific and comprehensive targeting of AACs facilitates the study of their developmental genetic program and circuit function across brain structures, providing a ground truth platform for understanding the conservation and variation of a bona fide cell type across brain regions and species.

Introduction

The precision of inhibitory control is crucial for regulating information processing and routing in brain circuits (Roux & Buzsáki, 2015). In the cerebral cortex, inhibitory signaling is mediated by a large array of GABAergic interneurons (INs), which regulate the input and output of glutamatergic projection neurons (PNs), together forming dynamic ensembles of information processing and relay. Cortical INs comprise highly diverse subpopulations distinguished by their anatomical and physiological properties and gene expression profiles (Fishell & Kepecs, 2020; Gouwens et al., 2020; Huang & Paul, 2019; Tremblay et al., 2016). Recent single-cell RNAseq and computational analyses have delineated the hierarchical tree-like organization of cortical GABAergic neurons from subclasses and supertypes down to transcriptomic subtypes (Tasic et al., 2018)(BICCN 2021). Among these, the axo-axonic cells (AACs), or chandelier cells (ChCs), represent the most distinctive and a bona fide type, as they exclusively innervate the axon initial segments (AIS) of pyramidal neurons (PNs) (Somogyi, 1977; Somogyi et al., 1982). Because AIS are the site of action potential initiation and individual AACs innervate hundreds of PNs in their vicinity, AACs are thought to exert decisive control over spike generation in ensembles of PNs (Crick 1986) (Howard et al., 2005), thereby regulating network operations and information relay. Thus, a more complete understanding of AACs will not only provide key insights into the functional organization of cortical circuits but also facilitate an integrated multi-modal definition of ground truth neuron types, shedding light on the granularity of hierarchical cell type organization. However, current knowledge on AAC distribution, connectivity, and function remains incomplete, largely due to the lack of reliable experimental tools.

An ideal genetic tool for studying AACs, or any other bona fide neuron type, would have two important features: specificity (targeting only AACs but no other cells) and comprehensiveness or even completeness (capturing most if not all AACs). Genetic labeling of AACs was first achieved through fate mapping neural progenitors of the medial ganglionic eminence (MGE) at late embryonic stages using the *Nkx2.1-CreER* mouse line (Taniguchi et al., 2013). This approach has facilitated analyses of neocortical AAC subtypes (Wang et al., 2019), transcriptome profiles (Paul et al., 2017), connectivity (Lu et al., 2017), synapse development (Ishino et al., 2017; Tai et al., 2019), and activity-dependent pruning (Wang et al., 2021); it also enabled a comprehensive fate mapping of AACs across MGE neurogenesis (Kelly et al., 2019). However, late embryonic induction in *Nkx2.1-CreER* mice is not only cumbersome but also not entirely specific to AACs (Kelly et al., 2019), and does not capture all AACs. With the identification of several putative AAC molecular markers from scRNAseq datasets (Paul et al., 2017; Tasic et al., 2018), several gene-knockin driver lines have been generated, which have facilitated studying AACs. Yet, none of these driver lines have been shown to be specific and comprehensive. For example, the *Vipr2-ires-Cre* driver captures a subset of neocortical and basolateral amygdala (BLA) AACs, but is not entirely specific in these areas (Daigle et al., 2018; Nakashima et al., 2022; Tasic et al., 2018). Similarly, our *Unc5b-CreER* line enabled AAV targeting of hippocampal AACs, but also labels endothelial cells when combined with a reporter line (Dudok et al., 2021). Despite extensive effort to date, no singularly unique molecular marker for AACs has been identified. Indeed, the same is true for most if not all neuronal subtypes of the mammalian brain. Therefore, specific and comprehensive genetic access to ground truth neuron types remains a broad and major challenge in neural circuit studies.

Here, we leverage lineage origin and molecular markers to establish an intersectional strategy, achieving highly specific and comprehensive targeting of AACs across the mouse brain. We discovered that much beyond the neocortex, hippocampus and BLA as previously described, AACs are in fact widely distributed across all pallium-derived brain structures and beyond. These include not only the dorsal pallium-derived neocortex and medial pallium-derived hippocampal formation, but also the lateral pallium-derived claustrum-insular complex, the ventral pallium-derived extended amygdaloid complex, and olfactory centers such as piriform cortex. In addition, putative AACs are also abundant in anterior olfactory nucleus, taenia tecta and are also found in the lateral septum and the diencephalic or third-ventricle-derived hypothalamus. The comprehensive labeling of cortical AACs allowed us to quantify their areal, laminar, and axon terminal distribution as well as to describe multiple anatomic subtypes. We further extend our strategy to AAV-based targeting and map synaptic input sources to AACs in sensorimotor cortical areas, hippocampal CA1, and BLA, demonstrating feasibility for functional manipulations. Together, these results provide a brain-wide overview of AACs and their subtype variations and input sources in the cerebral cortex. Precise and comprehensive genetic access to AACs sets the stage for understanding many aspects of their role in circuit development and function across the extended brain regions. This establishes a powerful model system to study the conservation and divergence of a ground truth neuron type across different brain regions towards understanding the principles of cell type organization.

Results

Lineage and marker-based intersectional targeting captures AACs across brain regions

The embryonic subpallium generates GABAergic neurons of the telencephalon, with the medial ganglionic eminence (MGE) giving rise to AACs (Kelly et al., 2019; Taniguchi et al., 2013) while other progenitor domains, such as the caudal ganglionic eminence (Miyoshi et al., 2015) or preoptic area (Gelman et al., 2011) do not. Within the MGE *Nkx2.1* lineage, AACs are generated in two consecutive waves during both early and late neurogenesis (Kelly et al., 2019), extending our initial report of their birth pattern (Taniguchi et al., 2013). Therefore, late embryonic induction in the *Nkx2.1-CreER* line only enriches a subset of neocortical AACs and also labels at least two other interneuron types (Kelly et al., 2019); this strategy also misses AACs in the hippocampus, BLA, and potentially other brain areas that are born earlier (Kelly et al. 2019). Taking a different approach based on scRNAseq analysis, we identified several putative AAC markers (Paul et al., 2017) and accordingly generated *Unc5b-CreER* and *Pthlh-Flp* driver lines. However, neither by itself is fully specific to AACs: the former also labels endothelial cells and sparse cortical pyramidal neurons (data not shown), and the latter labels a subset of CGE-derived interneurons (Figure 1—figure supplement 3m-p). To purify AACs from these driver lines, we then designed an intersectional strategy that combines lineage and molecular markers (Figure 1a); we tested the intersection of *Nkx2.1-Flp* with *Unc5b-CreER* as well as *Nkx2.1-Cre* with *Pthlh-Flp*. We expected that the constitutive *Nkx2.1-Flp* or *Cre* line would cover the entire output from MGE, including all AACs, and the intersection with postmitotic markers would specifically capture AACs.

We first combined *Nkx2.1-Flp* and *Unc5b-CreER* driver lines with an *Ai65* intersectional reporter allele to generate *Unc5b-CreER;Nkx2.1-Flp;Ai65* mice (Figure 1b). Tamoxifen induction (TM) allows dose-dependent titration of AAC labeling density, allowing the characterization of global

distribution patterns *en masse* with high dose as well as the evaluation of individual cell morphologies with sparser labeling by lower dose (see methods). Indeed, postnatal high dose TM induction generated dense and highly characteristic AAC labeling patterns throughout the neocortex, hippocampus, and BLA (Figure 1d-g). The characteristic chandelier axon arbor morphology with strings of synaptic boutons ("cartridges") along the AIS of pyramidal neurons unequivocally indicated their AAC identity (Figure 1, Figure 1—figure supplement 1-3).

Surprisingly, cell labeling extended much beyond these three previously reported structures that contain AACs. As the AAC identity of labeled cell are validated in most but not all these structures, we tentatively call some of these putative AACs (pAACs). Extensive analysis of these brain regions revealed an overarching pattern: AACs and pAACs are abundantly present in essentially all pallium-derived structures and several additional structures (Table 1; Figures 1c-g, Figure 1—figure supplement 1-2, Supplemental movie 1). The dorsal pallium (dPAL)-derived structures include the entire neocortex and entorhinal/ectorhinal cortices. The medial pallium (mPAL)-derived structures include the entire hippocampal formation. Beyond these previously known structures, pAACs are abundant in lateral pallium (lPAL)-derived claustrum, insular, and endopiriform dorsal. In addition, the ventral pallium (vPAL)-derived structures include most of the amygdaloid complex (cortical amygdala, basolateral and basomedial amygdala, and medial amygdala) and extended amygdala (bed nucleus of stria terminalis). Most surprisingly, AACs are highly abundant in a set of olfactory centers including piriform cortex, anterior olfactory nucleus, and taenia tecta. Among these, the piriform derives from the vPAL while AON and TTd derive from septum neuroepithelium. Finally, pAACs are found in lateral septum (also derived from septum neuroepithelium (Magno et al., 2022) and parts of the hypothalamus (derived largely from neuroepithelium of the third ventricle).

Consistent with these findings, the *Pthlh-Flp;Nkx2.1-Cre;Ai65* mice were found to have a similar overall pattern of pAAC distribution across different brain regions, with several differences (Figure 1—figure supplement 3). First, this intersection also labeled a set of layer 4 interneurons in the somatosensory cortex (Figure 1—figure supplement 3f). Second, *Pthlh;Nkx2.1* yielded slightly higher cell targeting in retrosplenial cortex (Figure 1—figure supplement 3h-i). Third, *Pthlh;Nkx2.1* labelled fewer cells in the AON and BST). As an additional application of the *Pthlh-Flp* line, we demonstrate that when combined with an inducible *Nkx2.1-CreER* driver (Taniguchi et al., 2013) the *Pthlh-Flp;Nkx2.1-CreER;Ai65* mice led to exclusive fate mapping of AACs (Figure 1—figure supplement 3j-l). The overall similarity between *Unc5b/Nkx2.1* and *Pthlh/Nkx2.1* patterns, and high density of cells captured, provided independent evidence that these intersectional approaches may have captured most if not all AACs in the brain.

In addition to targeting AACs, the *Pthlh-Flp* is a useful tool for at least two additional cell types. First, consistent with its expression in a set of CGE-derived interneurons (including VIP-expressing cells), intersection with the *VIP-Cre* driver line, which alone expresses in other cell types, was highly-specific for an interneuron subtype with striking vertical morphology that may represent interneuron-selective cells (Figure 1—figure supplement 3m-p). Second, *Pthlh/Nkx2.1* intersection yielded dense labeling of striatal interneurons (i.e. striatal neurons without axons in SNr/GPi)

(Figure 1—figure supplement 3f-h), consistent with known *Pthlh* expression in striatal PV interneurons (Munoz-Manchado et al., 2018).

In sum, our lineage and marker intersections combining *Nkx2.1-Flp/Cre,* or *CreER* with *Unc5b-CreER* or *Pthlh-Flp* appear to have achieved unprecedented specificity and comprehensiveness of AAC targeting. To validate this result, in the following sections, we present more detailed and quantitative descriptions of AACs and pAACs across brain structures.

Areal, laminar, and subtype distribution of AACs across the neocortex

Previous studies have identified ChCs in multiple neocortical areas and cortical layers with the observation of several morphological variants (Kelly et al., 2019; Somogyi et al., 1982; Taniguchi et al., 2013; Wang et al., 2019), but the global and quantitative distribution of ChC across the cerebral cortex and cortical layers is unknown. To first validate the specificity of our method to ChCs, we used single low dose TM induction to sparsely label individual cells across cortical areas (Figure 2—figure supplement 1). Combined with immunolabeling of AnkyrinG-stained pyramidal neuron (PN) AIS, we showed that the vast majority of RFP^+ cells (97.3%, n=110 cells from 6 mice) had axonal cartridge structure with synaptic boutons along PN AIS, validating their ChC identity (Figure 2—figure supplement 1).

To systematically map and quantify ChC distribution across the entire cerebral cortex, we then used high dose TM induction in *Unc5b-CreER;Nkx2.1-Flp;Ai65* mice to densely label ChCs and performed serial 2-photon tomography (STP) across the entire mouse brain at 50um intervals (Supplemental movie 1). The whole brain STP datasets were then registered to the Allen CCFv3 atlas, followed by segmentation of anatomical regions and an automated cell detection algorithm was applied to identify and quantify labeled cells in each region (Ragan et al., 2012; Kim et al., 2017; Matho et al., 2021). ChCs were detected across all areas of cerebral cortex (Figure 2a; Supplemental movie 1). Normalized cell density analysis revealed area-specific patterns (Figure 2b). The highest densities were observed in ventrolateral areas such as PERI, ECT, TEA, and AI as well as ventromedially in ILA (see appendix for abbreviations). There was a slight decline in ChC density very rostrally in FRP or caudally in RSP.

We further mapped ChC distribution across cortical layers in several sensory and motor areas (Figure 2c, d). The majority of ChC somas were located in L2/3, though this was area specific, with normalized density ranging from the lowest in SSs (65.5±0.6%) to highest in VISp (94.7±1.0%). An analysis of relative cortical depth (Figure 2e) revealed that ~80% of ChCs occupied a narrow band just below the L1/2 border, though this varied by anterior-posterior location. Nevertheless, ChCs were found at nearly all cortical depths, with a sizable proportion forming a second, less dense band above the white matter tract. This largely “bilaminar” pattern was highly evident in certain areas such as the SSp (Figure 2f).

To more systematically sample the morphological variations of ChCs, we used low dose TM induction to resolve individual cells across areas (Figure 2—figure supplement 1). We identified all the previously described laminar and morphological subtypes (Wang 2019), including supragranular

(L2/3) (Figure 2g), infragranular (L5/6) (Figure 2h), and inverted (axon arbors extend above cell soma). Notably, we found rather frequent bi-laminar and tri-laminar subtypes–L2/3 ChCs extending their axon arbors not only locally but further down to another one or two deep layers (Figure 2i). These translaminar ChCs may coordinate PN ensembles between cortical layers. The abundance of translaminar ChCs varied among cortical areas, e.g. with high abundance in auditory cortex (Figure 2j).

In addition to soma position and cell morphology, we sought to map the distribution of ChC axon terminals (i.e. cartridges) throughout the mouse cortex. For this purpose, we used a Cre/Flp-dependent reporter line expressing a synaptophysin-EGFP fusion protein and cytoplasmic tdTomato (Niederkofler et al., 2016) (Figure 2k-l). Following high-dose induction and dense labeling, we performed whole brain STP imaging and calculated cartridge density across ARAv3 areas (see Methods). ChC cartridges exhibited a wide range of densities across areas and layers (Figure 2m), with overall similarity to ChC soma densities in those areas and layers (Figure 2b). Plotting the relative laminar depth for ChC cartridges in each area (Figure 2n) revealed characteristic patterns of population-level laminar innervation onto PNs.

AACs in the hippocampus

Decades of studies of hippocampal AACs using traditional anatomical and physiological methods have implicated their role in network oscillations, including sharp waves and epilepsy (Fitzgerald et al., 2013; Klausberger et al., 2003; Viney et al., 2013) but the quantitative distribution of AACs across hippocampal formation has remained unknown, and reliable genetic access to hippocampal AACs is not well established. We applied *Unc5b/Nkx2.1* intersectional targeting and STP to map AAC distribution throughout hippocampal compartments. Single cell labeling by low-dose tamoxifen and immunohistochemistry confirmed that the vast majority (98.2%, n=56 cells, 6 mice) were AACs, characterized by vertically-oriented cross laminar apical dendrites in CA1-CA3 and axon terminals innervating PN AIS (Figure 3a-b, d). Dense labeling with high dose TM followed by cell density analysis revealed that AAC density was, surprisingly, highest in CA2 and lowest in dentate gyrus (Figure 3c), with density in CA1 and CA3 approximately equal. Only a very sparse population of AAC was labelled in dentate gyrus. Overall AAC density in CA2 was 3-4 fold greater than CA1/CA3 and 13-fold greater than DG (Figure 3c). As the density of PNs across hippocampal areas are overall similar, this result suggests substantially different AAC-PN innervation ratio and that AACs may exert much denser and likely stronger control of CA2 PNs than CA1/CA3 PNs or DG granule cells.

AACs in anterior insular, claustrum, and dorsal endopiriform nuclei

According to the updated tetrapartite model of pallial/cortical development (Figure 1c), the lateral pallium gives rise to the claustro-insular complex as well as the dorsal endopiriform nuclei (EPd) (Puelles, 2017). Our brain wide imaging of *Unc5b-CreER;Nkx2.1-Flp;Ai65* mice revealed pAACs deployed across these three regions (Figure 4a). Unlike cortical and hippocampal AACs whose axon arbors exhibit highly characteristic laminar pattern, reflecting the organization of their postsynaptic targets (i.e. AIS of PNs), the axon arbors of RFP cells in AI, CLA, EPd do not show clear laminar patterns and exhibit less uniformity and are more multipolar in morphology (Fig 4b-c), making it

more difficult to ascertain their identity. Nevertheless, strings of synaptic boutons were frequently identified that co-localized with AnkG labeled AIS, suggesting these as pAACs. Quantification from dense labeling revealed higher pAAC density in EPd compared to claustrum and EPv, the latter of which structure is derived from ventral pallium (Figure 4d).

AACs in the amygdaloid complex and extended amygdala

The amygdaloid complex includes over a dozen nuclei and can be segregated into 5 groups (Beyeler & Dabrowska, 2020): 1) the basolateral amygdala (BLA) divided into a dorsal section (lateral amygdala, LA) and basal section (basal amygdala, BA), 2) the basomedial amygdala (BMA), 3) the central amygdala (CeA) further splits into medial, lateral, and central sections (CeM, CeL, and CeC), 4) the medial amygdala (MeA), and 5) the cortical amygdala (CoA). Furthermore, the CeM extends rostrally and medially, thereby including the bed nucleus of stria terminalis (BST) to form the extended amygdala. Based on developmental origin, connectivity, and gene expression, these groups can be assigned into two large categories: pallium-derived cortex-like structures and subpallium-derived basal ganglia-like structures. The former includes BLA, CoA, BMA, and MeA, while the latter includes CeA and BST. Within the amygdala nuclei, projection neurons are exclusively glutamatergic in BLA, CoA, BMA, exclusively GABAergic in CeA, and predominantly GABAergic in MeA and BST. In rodents, there is also a population of GLU PNs (derived from third ventricle neuroepithelium) that populates the BST, MeA, and hypothalamus (Garcia-Moreno et al., 2010; Huilgol and Tole, 2016).

In this context, we found AACs or pAACs in all the amygdala nuclei containing GLU PNs, i.e. except CeA (Figure 4i-h). Sparse labelling and immunohistochemical co-staining with AnkG confirmed that the labeled cells in these compartments were nearly exclusively AIS-targeting (97.2%, n=36 cells, 6 mice). Morphologically, AACs in the amygdala tended to be similar to those in the claustrum, exhibiting multipolar dendrites and multipolar axon terminal branches (in contrast to axon arbor of cortical AACs that typically extend either below or above the soma) (Figure 4f). The density of AACs in amygdala appears to correlate with the known abundance of GLU PNs: densities in BLA, CoA, BMA were much higher than those in MeA and BST. Among the pallium-derived amygdala subdivisions (LA, BLA, BMA, PA), AACs were present at roughly similar densities (Figure 4i), while among striatum-like amygdala nuclei they were largely concentrated in MeA (Figure 4j). Our results indicate that AACs are deployed to all amygdala nuclei containing GLU PNs. Within the largely GABAergic structures such as MeA and BST, we hypothesize that pAACs might innervate the minor glutamatergic PNs in these structures.

AACs in olfactory centers: piriform cortex, AON, TTd

A major novel finding is the surprising abundance of AACs across multiple olfactory centers. Derived from the ventral pallium, the piriform cortex had been reported to contain axo-axonic synapses by co-localization of the inhibitory presynaptic marker GAT1 and AnkG (Wang and Sun, 2012). Our dense labelling in *Unc5b-CreER;Nkx2.1-Flp;Ai65* mice revealed a striking abundance of AACs that span the anterior-medial extent of the piriform in a single layer (Figure 5a-c). Sparse labeled single AACs exhibited characteristic morphologies analogous to L2/3 AACs of the neocortex, with extended branching of apical dendrites to L1 and dense axon arbors below the cell

body forming cartridges along PN AIS (Figure 5d-j). The single layer distribution pattern of piriform AACs continued dorsally to the insular cortex and ventrally to piriform-amygdala area (PAA) and COA (Figure 5c).

Furthermore, we found that AACs are deployed to two other olfactory centers that derive from outside of the four pallial domains: namely the anterior olfactory nucleus (AON) and taenia tecta (TT) (Figure 6a-b). Though exhibiting a range of different morphologies, AACs in all three areas resemble those of L2/3 neocortex, with apical dendrites often extending to the pia and basally-oriented axon arbors; their somata are located at the upper border of the pyramidal cell layer in the case of TT and AON (Figure 6c-g). Overall, AACs in piriform, TT, and AON exhibited higher density than AACs in cortex, hippocampus, and amygdala (Figure 6h, see Extended Data for Figures 2, 3, and 6).

AACs in the lateral septum

The LS, despite having no distinct laminar structure (delineated in ARAv3), shows some evidence of differential mRNA expression in superficial and deep domains, possibly analogous to a laminar organization (Besnard and Leroy, 2022). In *Unc5b-CreER;Nkx2.1-Flp;Ai65* mice, AACs tended to locate towards the midline (Figure 6b). Individual AACs were morphologically similar to cortical AACs, with extensive apical dendrites extending toward the midline and axon arbors and cartridges typically protruding away and into the cellular layer (Figure 6i-k).

Monosynaptic input tracing to AACs in sensorimotor cortex

In addition to using Cre AND Flp-dependent reporter lines for AAC access, it is advantageous to extend our intersectional strategy to engage viral vectors that enable more selective and anatomy-based labeling, recording, and manipulation. Because the endogenous expression of *Unc5b* and *Nkx2.1* occur at non-overlapping stages in development, it is not feasible to directly use Cre-AND-Flp dependent viral vectors (Fenno et al., 2020). Instead, we crossed *Unc5b-CreER;Nkx2.1-Flp* driver with a Cre-AND-Flp dependent tTA2 reporter line (Figure 7a) (Matho et al., 2021), which provides an indelible genetic handle for delivery of tTA-activated viral reporters. We tested this approach in AACs to map their synaptic input source by using tTA-activated AAVs in of *Unc5b-Cre;Nkx2.1-Flp;dual-tTA2* mice (Figure 7b; Figure 7 – Figure supplement 1b, c). We used the PV cell (PVC) population for comparison largely due to convenience, recognizing the fact that PVCs also include some ChCs.

We crossed the *dual-tTA2* reporter to either *Unc5b-CreER; Nkx2.1-Flp* or *PV-Cre; Nkx2.1-Flp* and performed monosynaptic input tracing to ChCs and PV cells (PVCs), respectively, in three sensorimotor areas: MOs, MOp, and SSp (Figure 7a-c, Figure 7 – Figure supplement 1a). Intersecting *PV-Cre* with *Nkx2.1-Flp* is a strategy for specifically targeting PV interneurons, as *PV-Cre* also captures a sparse population of excitatory pyramidal neurons (van brederode et al., 1991). Although PV is expressed in up to ~50% of cortical ChCs, starter cell depth distribution was found to be largely non-overlapping between injected ChCs and PVCs, likely due to the much higher abundance of PV basket cells (Figure 7d, Figure 7 – Figure supplement 1d-e).

Using serial two-photon tomography and our registration/cell detection pipeline, we mapped long-range inputs to different cortical ChC populations. Across sensorimotor cortex ChCs and PVCs integrated into highly-interconnected cortical networks. ChCs^{MOs} received ~50% of inputs from motor areas (41.0±2.3% in MOp, 4.5±0.7% in contra MOs) followed by SSp (20.4±4.2%) and SSs (9.5±0.7%) (Figure 7e). Long-range inputs to ChCs^{MOp} were largely dominated by sensory cortex (63.2±11.3% in SSp, 10.1±1.3% in SSs), followed by MOs (12.7±6.7%) and contra MOp (4.2±2.5%) (Figure 7f). In contrast, ChCs^{SSp} received only ~65% inputs total from sensorimotor (42.2±0.5% in SSs, 11.1±1.2% in MOs, 7.8±1.9% in MOp, 3.03±0.2% in contra SSp), with considerably more inputs from thalamus and other cortical areas (Figure 7g). Thalamocortical (TC) afferents to ChCs^{MOs} and ChCs^{MOp} were primarily from VAL, whereas TC inputs to ChCs^{SSp} were mostly from VPM. In addition to sensorimotor, other cortical areas such as ORB, FRP, AI, VIS, ACA, RSP, and AUD comprised a minor source of long-range inputs. Interestingly, we identified sparse inputs from GPe directly to ChCs and PV in all three cortical areas. Overall input patterns were comparable between ChCs and PV, although ChCs received significantly less homotypic inputs from the contralateral hemisphere for each injection site (Figure 7e-g).

Monosynaptic input tracing to AACs in CA1

The functional role of AACs is perhaps best understood in hippocampus, where CA3 AACs tend to fire at distinct epochs compared to other cell types and near the peak of theta oscillations (Viney et al., 2013). Little is known about the inputs to AACs that might drive this cell-type functional distinction, although non-specific tracers have identified an inhibitory connection from medial septum (MS) to AACs in CA3 (Viney et al., 2013). More recently, we used *Unc5b-CreER* to functionally characterize the firing patterns of AACs^{CA1} during whisking and locomotion (Dudok et al., 2021). Here, we applied cell type targeted retrograde monosynaptic tracing to map long-range inputs to AACs^{CA1} (Figure 8a-b).

Compared to cortical ChCs, AACs^{CA1} received inputs from more diverse sets of sources. Within the hippocampus formation, AACs^{CA1} received asymmetric inputs from each hemisphere, with relatively a higher fraction in CA3 contralaterally (29.0±2.4%) but higher ipsilaterally in DG (4.3±1.5%) and ENT (11.6±3.6%) and SUB (15.2±5.2%) (Figure 8c). Surprisingly, while the aforementioned study (Viney et al., 2013) found inhibitory connections from MS to AACs in CA3, we found in AACs^{CA1} over two-fold higher input connectivity from adjacent NDB (5.1±0.9%) compared to MS (2.0±0.2%). (Figure 8d-e). Immunohistochemistry analysis found the majority of these long-range inputs were inhibitory (56.8±4.8%) and a sizeable proportion ChAT-positive (27.6±4.0%) (Figure 8f-j). AACs^{CA1} also received diverse cortical inputs, including from VIS, RSP, AUD, SSp, PTLp, SSs, Tea, and PERI, as well as TC afferents from ATN (Figure 8l-p; see abbreviations in appendix).

Monosynaptic input tracing to AACs in basolateral amygdala

Comparatively little is known about the function or circuit role of AACs^{BLA}. Past studies have had to largely rely on post hoc identification from paired recordings, demonstrating their potent inhibitory effects (Veres et al., 2014). However, without cell type-specific tools for AACs^{BLA}, the long-range afferent connectivity that might drive these effects has remained virtually unknown. We applied our intersectional targeted approach to reveal the monosynaptic inputs to AACs^{BLA} (Figure 9a-b).

AACs^{BLA} received highly diverse sets of inputs (Figure 9c). AACs^{BLA} received strongest afferents from PIR (13.1±1.1%) and the hippocampal-entorhinal network (ENT 12.7±0.2%, CA1 10.5±2.0%, SUB 8.0±0.1%) (Figure 9e, h-i). The next strongest inputs originated from cortical amygdala areas (TR, PAA, COA) and cortical subplate nuclei (CeA, LA, EP, BMA) (Figure 9d). TC afferents were largely from MTN (2.6±0.4%), while cortical projections were identified in AI, AUD, PERI, ECT (Figure 9f). Input cells in LZ and MEZ of hypothalamus were found to be glutamatergic, while those from GPe and EP were GABAergic (Figure 9j-o).

Discussion

Specific and comprehensive targeting of ground truth cell types

A major challenge in studying the functional organization of GABAergic inhibitory circuits, and neural circuits in general, is establishing specific and comprehensive genetic access to ground truth cell types. Here, leveraging an intersectional strategy that integrates lineage and molecular markers, we have achieved near-perfect specificity and near-complete comprehensiveness in targeting a bona fide interneuron type. This strategy will facilitate studying the connectivity, function, and development of AACs across brain regions, thereby providing a robust experimental platform for integrating multi-modal analysis of a ground truth cell type across brain circuits. We recognize that it is currently not possible to fully assess the "completeness" of AAC targeting; this may require a comparison with complete labeling by anatomical ground truth, such as dense EM reconstruction of all AACs across the brain volume. Another practical drawback of our approach is the requirement of combining three engineered genetic alleles. In this context, the *Unc5b-CreER* line by itself is already useful for AAV-mediated targeting of AACs (Dudok et al., 2021). Because most AAVs are neurotrophic, Cre-activated AAVs would bypass endothelial cells to target only AACs in the *Unc5b-CreER* line, even though this approach is not suited to quantify brain-wide AAC patterns. Beyond relying on germline engineering, the recently invented CellREADR technology (Qian et al., 2022) will further simplify AAC targeting by identifying an RNA sensor of *Unc5b* mRNA and deliver it with an AAV vector. As *Unc5b* is a conserved AAC marker from rodents to primates including humans, the CellREADR approach may enable genetic access to AACs across mammalian species.

Implications of brain-wide AAC distribution pattern

The initial discovery of neocortical AACs was based on their striking chandelier-like morphology (Szentágothai, 1975), reflecting the spatial arrangement of their exclusive synaptic targets – the AIS of cortical pyramidal neurons (Somogyi, 1977; Somogyi et al., 1982). This defining feature of synapse specificity led to subsequent discoveries of AACs in the hippocampus and BLA. These findings have relied on meticulous efforts of skilled neuroanatomists to correctly identify AACs, mostly post hoc, by synapse specificity at AIS (Bienvenu et al., 2012; Veres et al., 2014). Since then, it has been widely assumed that AACs are restricted to these brain structures, and likely to the mammalian species. Here, based on developmental lineage and key molecular markers that likely include all AACs, our results reveal a vastly expanded and likely complete brain distribution pattern of AACs. Most importantly, we found that pAACs are deployed to the entire pallium-derived brain structures (Puelles, 2017), including not only the dPAL-derived neocortex and mPAL-derived hippocampal formation, but also the lPAL-derived claustrum-insular complex, the vPAL-derived extended amygdaloid complex, piriform cortex, and other olfactory centers such as AON, taenia tecta. In addition, subregions of the lateral septum and hypothalamus also contain pAACs.

Among the pallium-derived structures, the density of AACs vary substantially within and across regions. For example, within the neocortex, ChCs are highest in perirhinal and lowest in retrosplenial cortex. Across cortical layers, AACs are highly concentrated in L2, enriched in L5/6, and significantly less abundant in middle layers. Consistent with these results, the number and density of GABAergic synapses at AIS also vary substantially among different PyNs within and across cortical layers (DeFelipe et al., 1985; Fish et al., 2013; Schneider-Mizell et al., 2021). Similar variations are seen across the hippocampal formation, where CA2 exhibit the highest and DG the lowest density. It is also possible that these regional differences might reflect the distinction of PN types and/or their inherent physiological and connectivity properties that might require different levels and ratio of AAC control.

In particular, the finding of a striking abundance of AACs in olfactory centers across piriform cortex, AON, and taenia tecta suggests strong inhibitory regulation of PNs at AIS in these regions. Although the functional significance is not yet clear, the simpler circuit architecture and strong link to innate rodent behaviors of these olfactory centers may facilitate uncovering the logic of AAC function. Furthermore, as these olfactory circuits are evolutionarily preserved across vertebrate species (Zeppilli et al., 2023), our finding raises the possibility that AACs might be present in the CNS of other vertebrates, beyond the mammalian brain.

Notably, although the MeA and BST comprise mostly GABAergic neurons that are primarily generated from the subpallium, they contain subsets of glutamatergic projection neuron that migrate from pallium origin (Beyeler & Dabrowska, 2020) or from the third ventricle (Garcia-Moreno et al., 2010). The true AAC identity in these regions, and in several other regions such as the hypothalamus, remains to be validated by synapse innervation at AIS of GLU PNs. Nevertheless, based on current results, our overarching hypothesis is that AACs are deployed across all pallium-derived structures to control the AIS of GLU PNs, including those in MeA and BST. Our results also indicate that AACs are absent from the rest of the CNS. This finding suggests a major distinction between the physiology and functional organization of pallium-derived GLU PNs versus those in other CNS regions.

AACs as a model for understanding neuronal cell type organization across regions and species

The rapid scaling of single cell RNA sequencing enables the generation of massive transcriptome datasets across brain regions and species (Trygve E. Bakken et al., 2021; Hain et al., 2022). These datasets provide unprecedented opportunities to discover the organization and relationship of cell types within and across brain regions, which reflect their gene regulatory programs and developmental origin. Cross species analyses promise to further reveal the evolutionary conservation and divergence of brain cell types (T. E. Bakken et al., 2021; Tosches, 2021). However, transcriptomic cell homologies between brain regions and species, especially more distantly related regions and species, are often discernible only at a relatively coarse level and do not fully capture the biological complexity (Tosches, 2021). A major challenge is to evaluate statistically defined transcriptomic similarity against biological ground truth, such as anatomic connectivity and developmental relationship. In this context, the most appealing attribute of AACs is their singularly defining synapse specificity at AIS of GLU PNs, which can be readily measured and validated. Under this overarching connectivity-based definition, all other molecular and phenotypic variations can be assessed and organized accordingly regardless of brain regions and species. Therefore,

genetic access to AACs across brain regions provides a rare and compelling ground truth platform that can unambiguously identify this cell type across regions and species. This will further facilitate transcriptomic and epigenomic analysis to discover the gene regulatory program of AACs and contribute to understanding the principles of cell type organization by linking developmental genetic program, circuit connectivity and function, and evolutionary trajectory.

Acknowledgements

We thank P. Wu for generating the *Unc5b-CreER* and *Pthlh-Flp* mouse lines, R. Drewes for extensive support with STP imaging, K. Matho for help with cell detection and image analysis, S. George and L.Van Aelst for helpful discussions and providing antibodies, and S. Suryanarayana and D. Huilgol for extensive discussion and critical reading of the manuscript. We thank CSHL Animal Resources for mouse husbandry and Salk for providing rabies virus. This work was supported in part by the NIH grants 5R01MH094705-10, 5R01MH109665-05, and 5DP1MH129954-02 to Z.J.H; 5R01MH101214-08 and 2R01MH108924-06 to B.Li; and by the CSHL Robertson to Z.J.H. R.R. was supported by the NRSA F31 Predoctoral Fellowship 5F31MH114529-03 and A.P. by a NARSAD Post-doctoral Fellowship.

Author Contributions

Z.J.H. and B.L. conceived the study and obtained funding. Z.J.H. coordinated the study. Z.J.H., B.L., and R.R. designed the experiments. R.R., G. K., S.K., A.P., J.H., and S.Z. conducted mouse breeding, anatomy, immunohistochemistry, imaging and quantification. R.R. and W.G. performed virus injection experiments. R.R. and J.H. conducted whole-brain STP tomography and analysis of cell distribution patterns. S.Z. performed HCR ISH experiments. R.R. and Y.Q. generated the starter AAV virus. Z.J.H. and R.R. wrote the manuscript with contributions and edits from B.L. and S.K.

Figure Legends

Figure 1. Developmental genetic intersectional targeting reveals brain-wide AAC distribution patterns.

a) Schematic of lineage (*Nkx2.1*) and marker (*Unc5b*) intersection for pan-AAC labeling. Embryonic *Nkx2.1* expression defines MGE interneuron identity while subsequent postnatal *Unc5b* expression restricts interneurons to AACs. Height of green or gray shade represents relative expression levels.

b) Configuration of triple allele intersectional labeling, combining *Unc5b-CreER* and *Nkx2.1-Flp* drivers and the Cre-AND-Flp *Ai65* reporter. Embryonic Flp expression removes the frt-flanked STOP cassette and postnatal *Cre*ER induction removes the loxp-flanked STOP, thereby activating constitutive tdTomato expression.

c) Schematic showing that MGE-derived AACs migrate and populate all four pallial-derived brain structures depicted in color: medial pallium (red), dorsal pallium (green), lateral pallium (violet and blue), and ventral pallium (yellow and orange). Adapted from Puelles, 2017.

d) Representative midsagittal section showing AAC labeling in cerebral cortex, hippocampal formation (HPF), and olfactory centers such as piriform cortex (PIR) and anterior olfactory nucleus (AON). Note sparse labeling in lateral hypothalamus (LH) and striatum (str).

e-g) Representative coronal sections at specified anterior-posterior coordinates (from Bregma) showing dense AAC labelling in cerebral cortex (e-g), HPF (f-g), claustrum (CLA, e), endopiriform (EP, f,-g), taenia tecta (TTd, e), lateral septum (LS, e), basolateral amygdala (BLA, f-g), cortical amygdala (COA, f-g), medial amygdala (MeA, f), and hypothalamus (HYP, g). (Scale bars, 500µm.) Abbreviations for anatomical structures are listed in Appendix. All images showing Ai65-tdTomato were immunostained for signal amplification.

Figure 1 Supplement Figure 1. Dense labelling of AACs across brain regions in a *Unc5b-CreER;Nkx2.1-Flp;Ai65* mouse.

(a-f) Additional representative coronal sections showing dense Ai65 expression patterns at specified anterior-posterior coordinates (from Bregma). Note labeling in cerebral cortex (a-f); hippocampus (e-f); olfactory centers, including piriform, anterior olfactory nucleus, and tenia tecta dorsal (PIR, AON, TTd) (a-b); agranular insula, claustrum, and endopiriform nucleus (AI, CLA, EP) (b-c); amygdaloid complex and extended amygdala (COA, BLA, MeA) (d-f); Bed nuclei of the stria terminalis (BST) (d); and hypothalamus (HYP) (e-f). (Scale bars, 500µm.)

(g-j) Ai65-labelled pAACs in the bed nuclei of the stria terminalis (BST) are largely confined to the principal nucleus (BSTpr), with pAACs clustering more densely in anterior BSTpr (g-h) compared to more posterior segments (i-j).

(k-n) Ai65-labelled pAACs in the hypothalamus are densest in the ventral-medially area of the arcuate nucleus (ARH), with highest density in caudal portions (k-m) and more posteriorly in the paraventricular hypothalamic nuclei (PVP) (n). pAACs are also present sparsely in the dorsal-medial nucleus of the hypothalamus (DMH) (k-m).

Figure 1 Supplement Figure 2. Additional sagittal sections of *Unc5b-CreER; Nkx2.1-Flp; Ai65* mice highlighting dense pAACs in medial, lateral, and ventral pallium-derived structures.

(a-c) A lateral sagittal section showing the lPAL-derived anterior insular (AI), claustrum (CLA), endopiriform (EP) (magnified in b) and mPAL-derived hippocampal formation (magnified in c). Note the single-banded orientation of hippocampal (c) and insular (b) AACs that is absent in more inferior lPAL structures (b).

(d-e), A more medial sagittal section showing dorsal and ventral hippocampus and retrohippocampal region (RHP) (d), retrohippocampus, and visual and retrosplenial cortex (e). Compare the dual-banded AAC distribution in upper and deeper cortical layers to the single-banded pattern in hippocampus. Also note dense labeling in amygdaloid complex and extended amygdala (BLA, COA, and MeA) (a, d). (Scale bars, 500µm.)

Figure 1 Supplement Figure 3. Intersectional targeting with *Pthlh-Flp* and *Nkx2.1-Cre*, *Nkx2.1-CreER* or VIP-Cre to label specific subsets of AACs.

(a) Schematic of intersectional strategy.

(b-d) Tamoxifen induction of *Nkx2.1-CreER; Pthlh-Flp; Ai65* at E14.5 or E17.5 sparsely labels ChCs with diverse morphology in sensorimotor cortices. Arrowheads highlight a translaminar AAC type in layer 2, which extends axon arbors into deep layers. (Scale bars, 65µm.).

(e-i) Coronal hemisections from *Nkx2.1-Cre; Pthlh-Flp; Ai65* at specified anterior-posterior coordinates (mm from Bregma) showing pattern of dense labeling. Note labeling in cerebral cortex (e-i); hippocampus (h-i); olfactory centers, including piriform, anterior olfactory nucleus, and tenia tecta dorsal (e-h); agranular insula, claustrum, and endopiriform nucleus (AI, CLA, EP) (f); amygdaloid complex and extended amygdala (COA, BLA, MeA) (h-i); and hypothalamus (HYP) (i). Labeling by *Nkx2.1-Cre; Pthlh-Flp* is sparser in AON and anterior TTd and absent in BST compared to *Unc5b-CreER; Nkx2.1-Flp* (Fig1). Note non-AAC labeling of layer 4 interneurons in somatosensory cortex (g-h) and striatum (CP, f-h). The absence of projection fibers in SNr (i) suggests these striatal cells are not medium spiny neurons and likely striatal interneurons (Scale bars, 500µm.).

(j-l) Coronal hemisections from *Nkx2.1-CreER; Pthlh-Flp; Ai65* following a single tamoxifen dose at embryonic day 18.5 (E18.5) shows exclusive specificity for individual ChCs across neocortex (Scale bars, 500µm.)

(m) Intersectional strategy of *Pthlh* and *VIP* using *VIP-Cre;Pthlh-Flp; Ai65* mice.

(n-p) Dense labeling of cortical and hippocampal interneurons with predominantly bipolar morphology (putative interneuron-selective cells) in cortical layers II/III and deep layers (Scale bars, 500µm.)

Figure 2. Characterization of chandelier cells (ChCs, i.e. cortical AACs) in cerebral cortex.

(a) Representative 2D stereotactic plot of cortical ChC distribution in *Unc5b; Nkx2.1*. Dots represents individual RFP-labelled cells. Anterior-posterior distance from Bregma (vertical scale on right).

(b) Normalized ChC cell density (cells/um^3) following registration to ARAv3 isocortical areas. For b and c, data are mean ± SEM.

(c) Comparative bar plot showing relative proportion in each cortical layer in sensorimotor cortices.

(d) Violin plots of ChC cell density proportion along pia-to-white matter cortical depth in each sensorimotor cortical areas. Median is used for each violin plot.

(e) Scatterplot of ChC distribution along pia-to-white matter depth (vertical axis) and anterior-posterior distance from Bregma (horizontal axis, in mm); red dots represent individual cells. While a vast majority (~80%) of ChCs occupy a band near the layer I/II border, ChCs in other layers account for ~20% of the total cortical population and vary in depth distribution by anterior-posterior cortical location.

(f) Representative ChC laminar distribution pattern, showing largely separated supragranular (top inset) and infragranular (bottom inset) laminar subtypes. (Scale bars, 200µm and insets, 100 µm.)

(g-i) Multiple ChC laminar subtypes revealed by single-cell labeling using low-dose tamoxifen induction.

These include supragranular subtypes (g), infragranular and inverted subtypes (h), and translaminar L2/3 subtypes that extend long vertical axons (white arrowheads) to deep layers (i). White arrowheads highlight axonal plexi distant from soma in translaminar types. (Scale bars, 65µm.)

(j) Example of regional ChC morphological diversity in auditory cortex, with relatively high proportion of translaminar subtypes. (Scale bar, 200µm.)

(k-n) ChC axon terminal (i.e. “cartridge”) labeling and mapping using intersectional synaptophysin-EGFP/cytoplasmic-tdtomato reporter mouse line.

(k) Diagram of intersectional genetic labeling of ChC cartridges (EGFP) and soma (tdTomato).

(l) Pixel classifier trained to segment EGFP-expressing ChC cartridges in cortex and CA1 hippocampus. White arrowheads indicate detected EGFP-labelled cartridges. (Scale bars, 100µm).

(m) Density of ChC cartridges (cartridges/um^3) registered to ARAv3

(n) Representative relative depth plots (from pia) of individual detected cartridges at a single AP coordinate for each cortical area. Refer to Appendix for ARAv3 area label abbreviations. Note reduced deep layer cartridges in FRP, RSP, and V1.

Figure 2 Supplement Figure 1. Anatomical diversity of ChCs across neocortical areas.

AnkyrinG or IκBα immunohistochemical labeling (green) of PyN AIS was used for validation of axo-axonic targeting. Examples are shown of characteristic upper L2 ChCs in motor (a), sensory (b, d,j), cingulate (f, k), and insular cortex (i). Examples of deeper L5 or L6 ChCs in somatosensory (c,

e, g) and temporal association area (TEA) (h). Note the clustering of a distinct morphological subtypes in ventromedial infralimbic cortex (l). High-magnification inset (g): white arrowheads indicate segments of overlap between AnkG and RFP. Scale bars, 50µm and 5µm for high-magnification insets.

Figure 3. Distribution and validation of AACs in hippocampus.

(a) Population labeling of AACs throughout hippocampal compartments by *Unc5b; Nkx2.1* intersection. Note the highly-stereotyped banded distribution of AACs in CA1-CA3, with somata in the stratum pyramidale and vertically oriented dendrites extending basally to the stratum oriens and apically to the striatum lacunosum-moleculare. AACs are much sparser in dentate gyrus, with individual cells having elaborate and extended horizontal axon arbor. Scale bars, 200µm and 50µm for high-magnification inset.

(b) AACs in ventral CA1 have overall similar morphology as in dorsal CA1, though with longer basal-apical dendrites matching the ventral CA1 anatomy.

(c) Normalized AAC cell density (cells/um^3) across hippocampal compartments. CA2 has 3-4-fold higher AAC cell density compared to CA1 and CA3 and 12-fold higher compared to DG.

(d-i) Immunohistochemistry validation with the AIS markers AnkG or IκBα (green) and sparse-labelled RFP cells confirm axo-axonic targeting by the intersectional strategy. Examples of hippocampal AACs in CA1 (e, g), CA2 (d) and CA3 (d, f, h). In contrast, AACs in DG have much wider axon arbor in the stratum granulosum, potentially innervating many more granule cell AIS compared to in other hippocampal compartments (i). High-magnification inset: white arrowheads indicate segments of IκBα and RFP apposition. (Scale bars, 50µm and 20µm for high-magnification inset.) For b, data are mean ± SEM.

Figure 4. Distribution of AACs across lPAL- and vPAL-derived structures

(a) Dense labelled RFP cells in claustrum, endopiriform nucleus, and insula. Note AACs in insula follow the banded laminar pattern of AACs similar to cortical upper layers and piriform, while those in claustrum and endopiriform are more dispersed in distribution.

(b-c) Sparse labeling of single cell morphologies in endopiriform nucleus (b) and claustrum (c) showing elaborate dendritic and axonal branching structure. High-magnification insets: white arrowheads indicate segments of AnkG and RFP apposition. Scale bars, 50µm and 5µm for single cell examples and insets, respectively.

(d) Normalized AAC cell density (cells/um3) across lateral pallial structures. pAACs are approximately five-fold more prevalent in dorsal EP compared to ventral EP. Data are mean ± SEM.

(e) Dense labelling throughout vPall-derived amygdalar nuclei and piriform cortex. Note there is a degree of compartmentalization, with fewer cells in the ventral-most portions of EPd and the ventral BMA. The laminar pattern of AAC distribution in piriform and Piriform-amygdalar area (PAA) is similar to other three-layered allocortices.

(f-h) Immunohistochemistry of single cell labeling shows the multipolar morphologies characteristic of amygdalar AACs. High-magnification inset: white arrowheads indicate segments of AnkG and RFP apposition. (Scale bars, 500 µm for grayscale panels, 50µm and 5µm for single cell examples and insets.)

(i-j) Normalized AAC cell density (cells/um3) across cortical subplate (i) and striatum-like (j) amygdala. Data are mean ± SEM.

All images showing Ai65-tdTomato were immunostained for signal amplification, except for panels a and e which were native fluorescence.

Figure 5. AACs in piriform cortex.

(a-c) Dense AAC labelling in piriform cortex, organized from anterior (a) to posterior (c) and overlaid with ARAv3 area outlines. Note the highly laminar distribution patterns.

(d-j). Examples of single piriform AACs co-stained with AnkG (green). Note the relatively similar morphologies with only a few apical dendrites extending to the pial surface (d-g, i-j). An example of a deeper layer AAC at the border of piriform and EPv (h). White arrowheads in high-magnification insets indicate segments of overlap for RFP-labelled AAC and AnkG-labelled AIS. (Scale bars, 500µm for grayscale images, 50µm for confocal, 10µm for high-magnification insets.)

Figure 6. Identification and distribution of novel AAC subpopulations in anterior olfactory nucleus (AON), taenia tecta (TT), and septum.

(a-b) Dense population labeling in anterior AON and TT (a) and more posterior sections containing the TT and LS (b). Anteriorly, AACs are more concentrated in ventral TT while posteriorly in dorsal TT. Within LS, AACs tend to occupy the medial most portions along the midline.

(c-g, i-k) Single cell (confocal) labeling of AACs in anterior olfactory nucleus (c-d), taenia tecta (e-g), and lateral septum (i-k). Note that despite areal variations, individual AACs preserve their stereotyped morphological characteristics (apical-oriented dendrite and basal-oriented axon arbor) that conform to laminar patterns of targets in each anatomical area. High-magnification insets: white arrowheads indicate segments of AnkG and RFP apposition. (Scale bars, 200 µm for grayscale panels, 50µm and 5µm for single cell examples and insets.)

(h) Normalized cell density (cells/um^3) for AACs in AON, TT, and lateral septum. Within lateral septum, the majority of AACs are located in rostral compartments (LSr). Data are mean ± SEM.

Figure 7. Intersectional tTA2 conversion enables viral access and input tracing to ChCs in sensorimotor cortices.

(a) Schematic of intersectional tTA2-conversion strategy. Expression of *Nkx2.1-Flp* and subsequent *Unc5b-CreER* or *PV-Cre* results in activation of tTA2 expression in AACs. This provides a genetic handle for versatile viral targeting and manipulation.

(b) Cortical injection of TRE3G-promoter AAV vectors enables specific targeting of ChCs (green, left). A similar backbone was used to construct a TRE3G rabies starter AAV for monosynaptic input tracing, which contains both TVA and optimized rabies glycoprotein (right). Compared to TRE3G-EGFP, the TRE3G starter AAV has weaker EGFP labeling of neurites. (Scale bar, 200µm.)

(c) Linear regression fit of inputs cells/starter cells. Each point represents one animal, n= 18, r = 0.8874, slope = 135.51.

(d) Relative pia-to-white matter depth distribution of starter cells (expressing both AAV starter and rabies). ChC starter cell tended to cluster closer to the pia while PV cells were more broadly distributed throughout the cortical upper layers, reflecting the differences in the distribution of the two subtypes.

(e-g) Synaptic input source to ChCs in MOs, MOp, and SSp, with PV cells as comparison. Only long-range inputs (i.e. outside the ARAv3 area injected) are plotted.

Left: representative coronal sections from three indicated cortical areas overlaid with macroscale view of rabies tract labeling (in red, gray is autofluorescence) to each subpopulation of ChC.

Middle: Histogram comparing percentage of inputs from each structure innervating the indicated cortical subpopulation of ChCs (dark gray) and PV (light gray), sorted from largest input source to smallest. Inset: Representative top-down map of all inputs to AACs from a single animal.

Right: Representative sections highlighting select sources of rabies-labelled inputs to each ChC population, overlaid with ARAv3 boundaries. (Scale bars, 200µm.) For e-g, data are mean ± SEM, $^{**}P < 0.01$, $^{***}P < 0.001$, $^{****}P < 0.0001$ indicates $P \geq 0.05$ (two-way ANOVA with post hoc Bonferroni correction); for scatterplot in d, median is plotted. Homotypic projections to injection site from contralateral hemisphere are denoted by (#). All images showing EGFP were immunostained for signal amplification, while rabies-RFP shown in panels e-g were native fluorescence.

For each MOs, MOp and SSp, N=6 mice for (3 *Unc5b; Nkx2.1*, 3 *PV; Nkx2.1*; total N=18 mice)

Figure 7 Supplement Figure 1. Intersectional tTA2 conversion enables viral access and input tracing to ChCs and PV cells.

(a) Schematic and procedure for synaptic input tracing from ChC and PV interneurons. Top, driver and reporter lines to achieve tTA expression in ChC or PV cells. Middle, schematic of AAV and EnvA pseudo-typed rabies viral vectors. Bottom, timeline of tamoxifen and viral vector for retrograde synaptic tracing.

(b) Bulk injection of TRE3G-EGFP in *Unc5b-CreER; Nkx2.1-Flp; LSL-FSF-tTA2* results in efficient and specific labeling of ChCs, identifiable by laminar position and morphological features (inset). (Scale bars, 200µm and 100µm for high-magnification inset.)

(c) Starter AAV expression is comparable to TRE3G-EGFP with high specificity for ChCs in *Unc5b; Nkx2.1*, albeit with weaker EGFP neurite expression. (Scale bars, 100µm and 20µm for high-magnification insets.)

(d, e) Example of starter cells (arrowheads) co-expressing EGFP (AAV vector) and RFP (rabies vector) in *Unc5b/Nkx2.1* (d) and *PV/Nkx2.1* (e) intersections. (Scale bars, 100µm and 20µm for high-magnification insets.) All images showing EGFP were immunostained for signal amplification, while rabies-RFP shown in panels d-e were native fluorescence.

Figure 8. Monosynaptic input tracing to AACs^{CA1} of hippocampus.

(a) Schematic of retrograde synaptic tracing from CA1 AACs with site of viral injection.

(b) Starter AAV expression in CA1 (green). White arrowheads show soma position is largely confined to the pyramidal cell layer. (Scale bar, 50µm.)

(c) Comparative input distribution from ipsilateral (right) and contralateral (left) hippocampal compartments.

(d) Mesoscale rabies labeling of presynaptic input cells (red) to AACs^{CA1}

(e) Histogram of percentage of total inputs from each structure, sorted from largest to smallest. Inset: Summary schematic of input sources to AACs^{CA1}. AACs^{CA1}receive strong innervation from entorhinal, subiculum, and contralateral hippocampus, with more minor innervation from thalamus, medial septum, diagonal band nucleus, and various cortical areas.

(f-j) Immunohistochemistry and HCR RNA-FISH marker analysis of input cells in medial septum (MS) and nucleus of the diagonal band (NDB), indicated by color-coded labels. Examples of co-labeled cells are shown following HCR RNA-FISH for the inhibitory marker vGAT (g) and immunohistochemistry for the excitatory marker EAAC1 (h), PV (i) and ChAT (j). White arrowheads indicate co-labelled cells for each marker. (Scale bars, 50µm and 20µm for high-magnification insets.)

(k) Quantification of marker colocalization with rabies labeling in MS and NDB.

(l-p) Representative coronal sections highlighting select sources of rabies-labelled inputs to AACs^{CA1}, overlaid with ARAv3 atlas boundaries. Inputs within hippocampus were mostly from within CA1 both ipsilateral (l) and contralateral (m) to the injection site. Input cells were also found in adjacent cortical areas more posterior such as entorhinal cortex (ENT), auditory cortex (AUD), and temporal association area (TEa) (n-p). Thalamic inputs were largely confined to the anterior group of the dorsal thalamus (ATN) (o). (Scale bars, 200µm.)

For c, e, and k, data are mean ± SEM from N=4 mice. Homotypic projections to injection site from contralateral hemisphere are denoted by (#CA1) in e. EGFP in panel b and rabies-RFP in panels f-j were immunostained for signal amplification, while rabies-RFP shown in panels l-p were native fluorescence.

Figure 9. Monosynaptic input tracing to AACs^{BLA}.

(a) Schematic of retrograde synaptic tracing from BLA AACs with site of viral injection.

(b) Starter AAV distribution as indicated by white arrowheads, overlaid with ARAv3 atlas. (Scale bar, 200µm.)

(c) Left: Mesoscale rabies labeling of presynaptic input cells (red) to AACs^{BLA}. Right: Histogram of percentage of total inputs from each structure, sorted form largest to smallest. Inset: Summary schematic synaptic input source to AACs^{BLA}. AACs^{BLA} are innervated by diverse sets of inputs, with strongest innervation from entorhinal cortical-hippocampal network (EC-HPC), piriform areas (PIR), cortical subplate (CTXsp), and minor subcortical and cortical inputs.

(d-j) Representative coronal sections of rabies-labelled inputs (grey) across input structures, overlaid with ARAv3 boundaries. (Scale bars, 200µm.) Inputs to AACs^{BLA} were found in amygdalar and

cortical-amygdalar areas (d-e), piriform (e), midline group of the dorsal thalamus (f), substantia innominata (g), posterior hippocampus and cortex (h) and the ventral subiculum (i). Examples of dense input cells in medial (MEZ) and lateral (LZ) hypothalamus overlaid with excitatory vGLUT2 HCR RNA-FISH (j).

(k-o) Immunohistochemistry and RNA-FISH marker analysis of input cells in striatum/CP, GPe, EP, and hypothalamus. VGAT FISH or GABA IHC were used for identifying GABAergic input cells (l-n) while VGLUT2 FISH was used an excitatory marker (o) as indicated. White arrowheads indicate co-labelled cells. (Scale bars, 50µm and 20µm for high-magnification insets.) Right: Quantification of marker colocalization with rabies labeling for each corresponding area. Inputs to $AACs^{BLA}$ from CP, GPe, and EP were inhibitory, while inputs from hypothalamus were excitatory. Data are mean ± SEM from N=3 mice.

Rabies-RFP in panels j-o were immunostained for signal amplification, while EGFP in panel b and rabies-RFP shown in panels d-i were native fluorescence.

Materials and Methods

Key Resources Tables

Reagent type (species) or resource	Designation	Source or reference	Identifiers	Additional information
Antibody	Anti-AnkryinG (mouse monoclonal)	Neuromab	Cat#: 75-146	1:500
Antibody	Anti-ChAT (goat polyclonal)	Millipore	Cat#: AB144P	1:300
Antibody	Anti-EAAC1 (goat polyclonal)	Millipore	Cat#: AB1520	1:500
Antibody	Anti-GABA (rabbit polyclonal)	Sigma	Cat#: A2052	1:500
Antibody	Anti-GFP (chicken polyclonal)	Aves Labs	Cat#: 1020	1:1000
Antibody	Anti-parvalbumin (mouse monoclonal)	Sigma	Cat#: P3088	1:1000
Antibody	Anti-Phospho-IκBα (rabbit polyclonal)	Cell Signaling Technology	Cat#: 2859	1:500
Antibody	Anti-RFP (rabbit polyclonal)	Rockland	Cat#: 600-401-379	1:1000
Commercial assay or kit	HCR v3.0	Molecular Instruments		
Other	AAVDJ-TRE3g-EGFP	Vigene		Adeno-associated virus, titer: 5 × 1012 genome copies (gc)/ml
Other	AAVDJ-TRE3g-TVA-oG-EGFP	Vigene		Adeno-associated virus, titer: 9.24 × 1012 genome copies (gc)/ml
Other	G-Deleted Rabies dsRedXpress	Salk Institute		Rabies virus, titer: 5.0 × 10^7 colony-forming units (cfu)/ml
Software, algorithm	ImageJ	NIH	RRID:SCR_003070	
Software, algorithm	MATLAB	Mathworks	R2017b RRID:SCR_001622	
Strain (Mus musculus)	Ai65	The Jackson Laboratory	021875 RRID:IMSR_JAX:021875	
Strain (Mus musculus)	C57BL/6J	The Jackson Laboratory	000664 RRID:IMSR_JAX:000664	

Strain (Mus musculus)	dual-SynaptotagminEGFP-2A-tdTomato	The Jackson Laboratory	030206 RRID:IMSR_JAX:030206	
Strain (Mus musculus)	dual-tTA2	The Jackson Laboratory	036304 RRID:IMSR_JAX:036304	
Strain (Mus musculus)	Nkx2.1-Cre	The Jackson Laboratory	008661 RRID:IMSR_JAX:008661	
Strain (Mus musculus)	Nkx2.1-FlpO	The Jackson Laboratory	028577 RRID:IMSR_JAX:028577	
Strain (Mus musculus)	Pthlh-FlpO			
Strain (Mus musculus)	PV-Cre	The Jackson Laboratory	017320 RRID:IMSR_JAX:017320	
Strain (Mus musculus)	Unc5b-CreER			

Animals

All experiments were carried out in accordance with the guidelines of the Animal Care and Use Committee of Cold Spring Harbor Laboratory (CSHL). Mice were housed in groups of five per cage or singly if pregnant under standard vivarium conditions with a 12 h light/dark cycle. Unc5b-CreER (Dudok et al., 2021) or PV-Cre (JAX, Stock 017320) were crossed to Nkx2.1-Flp (JAX, Stock 028577). Pthlh-Flp (unpublished) was crossed to Nkx2.1-Cre (JAX, Stock 008661). For each Cre/Flp combination, offspring hemizygous for both alleles were crossed to Ai65 (JAX, Stock 021875), Rosa26-loxpSTOPloxp-frtSTOPfrt-synaptotagminEGFP-2A-tdTomato (JAX, Stock 030206), or Rosa26-loxpSTOPloxp-frtSTOPfrt-tTA2 (JAX, Stock 036304) reporter mice. Mice with Unc5b-CreER were induced by tamoxifen i.p. (TM; Sigma-Aldrich, Cat# T5648) administered either 1) for dense labelling and input tracing, 100mg/kg for five consecutive days starting at P55-60 2) for single cell labeling, 25mg/kg for 1-2 consecutive days at P55-P60. The dosage and regimen of tamoxifen for dense AAC labelling was the maximum based on established protocols for conditional knockouts and one that was well-tolerated. For single cell labeling, the tamoxifen dosage was determined empirically for reliable labeling of non-overlapping AACs in different brain areas. Animals were fed ad libitum and their health status were routinely monitored. Both male and female animals were used in all experiments, with 3-4 mice total for each injection site x genotype and for cell distribution analysis. Genotyping was performed using PCR and according to supplier protocols.

Immunohistochemistry

Mice were anesthetized with Avertin and transcardially perfused with 0.9% saline followed by 4% paraformaldehyde in 0.1M phosphate buffer. Following overnight post-fixation, brains were rinsed in PBS and sectioned at 50-65µm thickness with a Leica VT1000S vibratome. For immunohistochemistry, sections were first treated with a secondary-matched blocking solution (10% normal goat or donkey serum and 0.2% Triton-X100 in PBS) for 1 hr, then incubated overnight at 4°C with primary antibodies diluted in 5% blocking solution. Sections were washed three times in PBS and incubated for 2h at room temperature with corresponding secondary antibodies, Goat or

Donkey Alexa Fluor 488, 568 or 647 (1:500, Life Technologies) and DAPI to label nuclei (1:1000 in PBS, Life Technologies, Cat# 33342). Sections were washed three times with PBS and dry-mounted on slides using Fluoromount-G (SouthernBiotech, Cat# 0100-01) mounting medium. Primary antibodies used were Anti-AnkryinG (1:500, Neuromab, Cat#: 75-146), Anti-ChAT (1:300, Millipore, Cat#: AB144P), Anti-EAAC1 (1:500, Millipore, Cat#: AB1520), Anti-GABA (1:500, Sigma-Aldrich, Cat#: A2052), Anti-GFP (1:1000, Aves Labs, Cat#: 1020), Anti-parvalbumin (1:1000, Sigma-Aldrich, Cat#: P3088), Anti-Phospho-IκBα (1:500, Cell Signaling Technology, Cat#: 2859), Anti-RFP (1:1000, Rockland, Cat#: 600-401-379). Samples for AAC validation were collected from 6 mice given 25mg/kg for 1-2 consecutive days, as described above. Validation was conducted with high-magnification confocal microscopy and defined by a cell exhibiting at least two RFP-labelled axons colocalized with AIS labelled by AnkryinG or Phospho-IκBα.

Floating section two-color in situ hybridization

In situ hybridization was performed using hybridization chain reaction (HCR v3.0, Molecular Instruments). Samples post-fixed in 4% PFA at 4°C were cryoprotected in 30% sucrose solution in RNAse-free PBS (DEPC-PBS) at 4°C for 48 hr, frozen in Tissue-Tek O.C.T. Compound (Sakura), and stored at –80°C until sectioning. 50 µm thick coronal floating sections were collected into a sterile 24-well plate in DEPC-PBS, fixed again briefly for 5 min in 4% PFA, then placed in 70% EtOH in DEPC-PBS overnight. Sections were rinsed in DEPC-PBS, incubated for 45 min in 5% SDS in DEPC-PBS, rinsed and incubated in 2x SSCT, pre-incubated in HCR hybridization buffer at 37°C, and then placed in HCR hybridization buffer containing RNA probes overnight at 37°C. The next day, sections were rinsed 4 × 15 min at 37°C in HCR probe wash buffer, rinsed with 2X SSCT, pre-incubated with HCR amplification buffer, then incubated in HCR amplification buffer containing HCR amplifiers at room temperature for ~24 hr. On the final day, sections were rinsed in 2x SSCT, rinsed again with 2x SSCT, then mounted on slides and coverslipped with Fluoromount-G (Southern Biotech).

Microcopy and image analysis

Confocal imaging was performed on a Zeiss LSM 780 (CSHL St. Giles Advanced Microscopy Center) using 10x, 20x, or 63x objectives. Imaging for grayscale overview images was performed on a Zeiss Axioimager M2 System equipped with MBF Neurolucida Software (MBF) using 5x, 10x, or 20x objectives. Quantification and image analysis was performed using Image J/FIJI software. Statistics and plotting of graphs were done using GraphPad Prism 7 and Microsoft Excel 2010. All images shown in figures were acquired by one-photon microscopy (confocal, epifluorescence) with the exception of Figure 1 Supplement Figure 1 panels g-n, Figure 7 panels e-g, Figure 8 panels l-p, and Figure 9 panels d-i, which were acquired by serial two-photon tomography.

Viruses

To construct AAVDJ-TRE3g-TVA-oG-eGFP, TVA, the optimized rabies glycoprotein oG (Kim et al., 2016), and eGFP were linked by 'self-cleaving' 2A and P2A peptides and cloned into pAAV-TRE3G (Sacha Nelson). For AAVDJ-TRE3g-eGFP only eGFP was cloned. AAVs serotype DJ were packaged by a commercial vector core facility (Vigene). Genomic titers of AAVDJ-TRE3g-TVA-oG-eGFP and AAVDJ-TRE3g-eGFP were 9.24×10^{12} gc/ml and 5.0×10^{12} gc/ml, respectively. TVA, oG, and eGFP were subcloned from AAV-hSyn-FLEX-TVA-P2A-EGFP-2A-oG (Addgene, Cat# 85225). AAVs were diluted 1:5 in 1x PBS immediately prior to use. EnvA-pseudotyped G-Deleted Rabies dsRedXpress was purchased from Salk Institute (5.0 × 10^7 titer units (TU)/ml).

Stereotactic viral injections

Adult mice were anaesthetized with 2% isofluorane delivered by constant air flow (0.4 L/min). Analgesics ketoprofen (5 mg/kg) and dexamethasone (0.5 mg/kg) were administered subcutaneously just prior to sugery, while lidocaine (2-4 mg/kg) was applied intra-inciscionally. Mice were mounted on a stereotaxic headframe (Kopf Instruments, 940 series or Leica Biosystems, Angle Two) and stereotactic coordinates identified as follows, (MOs): 2.25mm anterior to bregma, 1.2mm lateral, 0.3mm in depth; (MOp): 0.5mm anterior to bregma, 1.6mm lateral, 0.3mm in depth; (SSp): 1.12mm posterior to bregma, 3.25mm lateral, 0.3mm in depth; (CA1): 1.94mm posterior to bregma, 1.4mm lateral, 1.4mm in depth ; (BLA): 1.9mm posterior to bregma, 3.38mm lateral, 4.76mm in depth. An incision was made over the scalp, a small burr hole drilled in the skull and brain surface exposed. A pulled glass pipette with a tip of 20–30 µm containing virus was lowered into the brain. Virus was delivered at a rate of 30nL/min using a Picospritzer (General Valve Corp) for a total volume of 100-150nL for starter AAV and 300-400nL for rabies virus. The pipette remained in place for 10 min prior to retraction to prevent backflow, after which the incision was closed with 5/0 nylon suture thread (Ethilon Nylon Suture Ethicon) or Tissueglue (3M Vetbond). Mice were kept warm on a heating pad until complete recovery. For input tracing experiments, *Unc5b-CreER; Nkx2.1-Flp; dual-tTA2* (tamoxifen-induced as described above) and *PV-Cre; Nkx2.1-Flp; dual-tTA2* were injected at respective coordinates with AAVDJ-TRE3g-TVA-oG-eGFP at P75±2. After a 2-3 week incubation period, a second injection at the same coordinates was performed using EnvA-pseudotyped G-Deleted Rabies-dsRedXpress. Following another 7 day incubation mice were perfused as described above.

Whole-brain STP tomography and image analysis

We used the whole-brain STP tomography pipeline described previously (Ragan et al., 2012; Kim et al., 2017; Matho et al., 2021). Perfused and post-fixed brains were embedded in 4% oxidized-agarose in 0.05 M PB, cross-linked in 0.2% sodium borohydrate solution (in 0.05 M sodium borate buffer, pH 9.0–9.5). The entire brain was imaged coronally with a 20× Olympus XLUMPLFLN20XW lens (NA 1.0) on a TissueCyte 1000 (Tissuevision) with a Chameleon Ultrafast-2 Ti:Sapphire laser (Coherent). EGFP/EYFP or tdTomato/dsRedXpress signals were excited at 910 nm or 920 nm, respectively. Whole-brain image sets were acquired as series of 12 (x) × 16 (y) tiles with 1 µm × 1 µm sampling for 230–270 z sections with a 50-µm z-step size. Images were collected by two PMTs (PMT, Hamamatsu, R3896), for signal and autofluorescent background, using a 560-nm dichroic mirror (Chroma, T560LPXR) and band-pass filters (Semrock FF01-680/SP-25). The image tiles were corrected to remove illumination artifacts along the edges and stitched as a grid sequence. Image processing was completed using ImageJ/FIJI and Adobe/Photoshop software with linear level and nonlinear curve adjustments applied only to entire images. Registration of brain-wide datasets to the Allen reference Common Coordinate Framework version 3 (CCFv3) was performed by 3D affine registration followed by a 3D B-spline registration using Elastix software (Klein et al., 2010), according to established parameters. Somata labelled by Ai65-tdtomato or rabies-dsRedXpress and catridges labelled by synaptotagmin-EGFP were automatically detected by a convolutional network trained as described previously (Ragan et al., 2012; Kim et al., 2017; Matho et al., 2021). For AAC laminar depth, somata and cartridge coordinates were overlaid on a mask for relative cortical depth, as described. For area cell density and cortical depth analysis, we registered each dataset, reporting cells detected in each brain structure without warping the imaging channel. For rabies input tracing experiments, only inputs originating outside the ARAv3 area injected were plotted (i.e. only long-range inputs). All cell density quantifications are reported as mean cells per cubic µm ± SEM from n=4 mice.

Data availability

The data that support the findings of this study are presented in Source data 1.

References

Bakken, T. E., Jorstad, N. L., Hu, Q., Lake, B. B., Tian, W., Kalmbach, B. E., Crow, M., Hodge, R. D., Krienen, F. M., Sorensen, S. A., Eggermont, J., Yao, Z., Aevermann, B. D., Aldridge, A. I., Bartlett, A., Bertagnolli, D., Casper, T., Castanon, R. G., Crichton, K., . . . Lein, E. S. (2021). Comparative cellular analysis of motor cortex in human, marmoset and mouse. *Nature*, *598*(7879), 111-119. https://doi.org/10.1038/s41586-021-03465-8

Bakken, T. E., Jorstad, N. L., Hu, Q., Lake, B. B., Tian, W., Kalmbach, B. E., Crow, M., Hodge, R. D., Krienen, F. M., Sorensen, S. A., Eggermont, J., Yao, Z., Aevermann, B. D., Aldridge, A. I., Bartlett, A., Bertagnolli, D., Casper, T., Castanon, R. G., Crichton, K., . . . Lein, E. S. (2021). Comparative cellular analysis of motor cortex in human, marmoset and mouse. *Nature*, *598*(7879), 111-119. https://doi.org/10.1038/s41586-021-03465-8

Beyeler, A., & Dabrowska, J. (2020). Neuronal diversity of the amygdala and the bed nucleus of the stria terminalis. *Handb Behav Neurosci*, *26*, 63-100. https://doi.org/10.1016/b978-0-12-815134-1.00003-9

Bienvenu, T. C., Busti, D., Magill, P. J., Ferraguti, F., & Capogna, M. (2012). Cell-type-specific recruitment of amygdala interneurons to hippocampal theta rhythm and noxious stimuli in vivo. *Neuron*, *74*(6), 1059-1074. https://doi.org/10.1016/j.neuron.2012.04.022

Daigle, T. L., Madisen, L., Hage, T. A., Valley, M. T., Knoblich, U., Larsen, R. S., Takeno, M. M., Huang, L., Gu, H., Larsen, R., Mills, M., Bosma-Moody, A., Siverts, L. A., Walker, M., Graybuck, L. T., Yao, Z., Fong, O., Nguyen, T. N., Garren, E., . . . Zeng, H. (2018). A Suite of Transgenic Driver and Reporter Mouse Lines with Enhanced Brain-Cell-Type Targeting and Functionality. *Cell*, *174*(2), 465-480.e422. https://doi.org/10.1016/j.cell.2018.06.035

DeFelipe, J., Hendry, S. H., Jones, E. G., & Schmechel, D. (1985). Variability in the terminations of GABAergic chandelier cell axons on initial segments of pyramidal cell axons in the monkey sensory-motor cortex. *J Comp Neurol*, *231*(3), 364-384. https://doi.org/10.1002/cne.902310307

Dudok, B., Szoboszlay, M., Paul, A., Klein, P. M., Liao, Z., Hwaun, E., Szabo, G. G., Geiller, T., Vancura, B., Wang, B.-S., McKenzie, S., Homidan, J., Klaver, L. M. F., English, D. F., Huang, Z. J., Buzsáki, G., Losonczy, A., & Soltesz, I. (2021). Recruitment and inhibitory action of hippocampal axo-axonic cells during behavior. *Neuron*, *109*(23), 3838-3850.e3838. https://doi.org/10.1016/j.neuron.2021.09.033

Fenno, L. E., Ramakrishnan, C., Kim, Y. S., Evans, K. E., Lo, M., Vesuna, S., Inoue, M., Cheung, K. Y. M., Yuen, E., Pichamoorthy, N., Hong, A. S. O., & Deisseroth, K. (2020). Comprehensive Dual- and Triple-Feature Intersectional Single-Vector Delivery of Diverse Functional Payloads to Cells of Behaving Mammals. *Neuron*, *107*(5), 836-853 e811. https://doi.org/10.1016/j.neuron.2020.06.003

Fish, K. N., Hoftman, G. D., Sheikh, W., Kitchens, M., & Lewis, D. A. (2013). Parvalbumin-containing chandelier and basket cell boutons have distinctive modes of maturation in monkey prefrontal cortex. *J Neurosci*, *33*(19), 8352-8358. https://doi.org/10.1523/JNEUROSCI.0306-13.2013

Fishell, G., & Kepecs, A. (2020). Interneuron Types as Attractors and Controllers. *Annual Review of Neuroscience*, *43*(1), 1-30. https://doi.org/10.1146/annurev-neuro-070918-050421

Fitzgerald, T. H., Valentin, A., Selway, R., & Richardson, M. P. (2013). Cross-frequency coupling within and between the human thalamus and neocortex. *Front Hum Neurosci*, *7*, 84. https://doi.org/10.3389/fnhum.2013.00084

Garcia-Moreno, F., Pedraza, M., Di Giovannantonio, L. G., Di Salvio, M., Lopez-Mascaraque, L., Simeone, A., & De Carlos, J. A. (2010). A neuronal migratory pathway crossing from diencephalon to telencephalon populates amygdala nuclei. *Nature Neuroscience*, *13*(6), 680-689. https://doi.org/10.1038/nn.2556

Gelman, D., Griveau, A., Dehorter, N., Teissier, A., Varela, C., Pla, R., Pierani, A., & Marin, O. (2011). A wide diversity of cortical GABAergic interneurons derives from the embryonic preoptic area. *J Neurosci*, *31*(46), 16570-16580. https://doi.org/10.1523/JNEUROSCI.4068-11.2011

Gouwens, N. W., Sorensen, S. A., Baftizadeh, F., Budzillo, A., Lee, B. R., Jarsky, T., Alfiler, L., Baker, K., Barkan, E., Berry, K., Bertagnolli, D., Bickley, K., Bomben, J., Braun, T., Brouner, K., Casper, T., Crichton, K.,

Daigle, T. L., Dalley, R., . . . Zeng, H. (2020). Integrated Morphoelectric and Transcriptomic Classification of Cortical GABAergic Cells. *Cell*, *183*(4), 935-953 e919. https://doi.org/10.1016/j.cell.2020.09.057

Hain, D., Gallego-Flores, T., Klinkmann, M., Macias, A., Ciirdaeva, E., Arends, A., Thum, C., Tushev, G., Kretschmer, F., Tosches, M. A., & Laurent, G. (2022). Molecular diversity and evolution of neuron types in the amniote brain. *Science*, *377*(6610), eabp8202. https://doi.org/10.1126/science.abp8202

Howard, A., Tamas, G., & Soltesz, I. (2005). Lighting the chandelier: new vistas for axo-axonic cells. *Trends Neurosci*, *28*(6), 310-316. https://doi.org/10.1016/j.tins.2005.04.004

Huang, Z. J., & Paul, A. (2019). The diversity of GABAergic neurons and neural communication elements. *Nature Reviews Neuroscience*, *20*(9), 563-572. https://doi.org/10.1038/s41583-019-0195-4

Ishino, Y., Yetman, M. J., Sossi, S. M., Steinecke, A., Hayano, Y., & Taniguchi, H. (2017). Regional Cellular Environment Shapes Phenotypic Variations of Hippocampal and Neocortical Chandelier Cells. *The Journal of Neuroscience*, *37*(41), 9901-9916. https://doi.org/10.1523/jneurosci.0047-17.2017

Kelly, S. M., Raudales, R., Moissidis, M., Kim, G., & Huang, Z. J. (2019). *Multipotent radial glia progenitors and fate-restricted intermediate progenitors sequentially generate diverse cortical interneuron types* [preprint]. http://biorxiv.org/lookup/doi/10.1101/735019

Klausberger, T., Magill, P. J., Márton, L. F., Roberts, J. D. B., Cobden, P. M., Buzsáki, G., & Somogyi, P. (2003). Brain-state- and cell-type-specific firing of hippocampal interneurons in vivo. *Nature*, *421*(6925), 844-848. https://doi.org/10.1038/nature01374

Lu, J., Tucciarone, J., Padilla-Coreano, N., He, M., Gordon, J. A., & Huang, Z. J. (2017). Selective inhibitory control of pyramidal neuron ensembles and cortical subnetworks by chandelier cells. *Nature Neuroscience*, *20*(10), 1377-1383. https://doi.org/10.1038/nn.4624

Magno, L., Asgarian, Z., Apanaviciute, M., Milner, Y., Bengoa-Vergniory, N., Rubin, A. N., & Kessaris, N. (2022). Fate mapping reveals mixed embryonic origin and unique developmental codes of mouse forebrain septal neurons. *Commun Biol*, *5*(1), 1137. https://doi.org/10.1038/s42003-022-04066-5

Miyoshi, G., Young, A., Petros, T., Karayannis, T., McKenzie Chang, M., Lavado, A., Iwano, T., Nakajima, M., Taniguchi, H., Huang, Z. J., Heintz, N., Oliver, G., Matsuzaki, F., Machold, R. P., & Fishell, G. (2015). Prox1 Regulates the Subtype-Specific Development of Caudal Ganglionic Eminence-Derived GABAergic Cortical Interneurons. *J Neurosci*, *35*(37), 12869-12889. https://doi.org/10.1523/JNEUROSCI.1164-15.2015

Munoz-Manchado, A. B., Bengtsson Gonzales, C., Zeisel, A., Munguba, H., Bekkouche, B., Skene, N. G., Lonnerberg, P., Ryge, J., Harris, K. D., Linnarsson, S., & Hjerling-Leffler, J. (2018). Diversity of Interneurons in the Dorsal Striatum Revealed by Single-Cell RNA Sequencing and PatchSeq. *Cell Rep*, *24*(8), 2179-2190 e2177. https://doi.org/10.1016/j.celrep.2018.07.053

Nakashima, M., Ikegaya, Y., & Morikawa, S. (2022). Genetic labeling of axo-axonic cells in the basolateral amygdala. *Neuroscience Research*, *178*, 33-40. https://doi.org/10.1016/j.neures.2022.02.002

Paul, A., Crow, M., Raudales, R., He, M., Gillis, J., & Huang, Z. J. (2017). Transcriptional Architecture of Synaptic Communication Delineates GABAergic Neuron Identity. *Cell*, *171*(3), 522-539.e520. https://doi.org/10.1016/j.cell.2017.08.032

Puelles, L. (2017). Comments on the Updated Tetrapartite Pallium Model in the Mouse and Chick, Featuring a Homologous Claustro-Insular Complex. *Brain Behav Evol*, *90*(2), 171-189. https://doi.org/10.1159/000479782

Qian, Y., Li, J., Zhao, S., Matthews, E. A., Adoff, M., Zhong, W., An, X., Yeo, M., Park, C., Yang, X., Wang, B. S., Southwell, D. G., & Huang, Z. J. (2022). Programmable RNA sensing for cell monitoring and manipulation. *Nature*, *610*(7933), 713-721. https://doi.org/10.1038/s41586-022-05280-1

Roux, L., & Buzsáki, G. (2015). Tasks for inhibitory interneurons in intact brain circuits. *Neuropharmacology*, *88*, 10-23. https://doi.org/10.1016/j.neuropharm.2014.09.011

Schneider-Mizell, C. M., Bodor, A. L., Collman, F., Brittain, D., Bleckert, A., Dorkenwald, S., Turner, N. L., Macrina, T., Lee, K., Lu, R., Wu, J., Zhuang, J., Nandi, A., Hu, B., Buchanan, J., Takeno, M. M., Torres, R., Mahalingam, G., Bumbarger, D. J., . . . Costa, N. M. D. (2021). Structure and function of axo-axonic inhibition. *eLife*, *10*. https://doi.org/10.7554/eLife.73783

Somogyi, P. (1977). A specific 'axo-axonal' interneuron in the visual cortex of the rat. *Brain Research*, *136*(2), 345-350. https://doi.org/10.1016/0006-8993(77)90808-3

Somogyi, P., Freund, T. F., & Cowey, A. (1982). The axo-axonic interneuron in the cerebral cortex of the rat, cat and monkey. *Neuroscience*, *7*(11), 2577-2607. https://doi.org/10.1016/0306-4522(82)90086-0

Szentágothai, J. (1975). The 'module-concept' in cerebral cortex architecture. *Brain Research*, *95*(2-3), 475-496. https://doi.org/10.1016/0006-8993(75)90122-5

Tai, Y., Gallo, N. B., Wang, M., Yu, J.-R., & Van Aelst, L. (2019). Axo-axonic Innervation of Neocortical Pyramidal Neurons by GABAergic Chandelier Cells Requires AnkyrinG-Associated L1CAM. *Neuron*, *102*(2), 358-372.e359. https://doi.org/10.1016/j.neuron.2019.02.009

Taniguchi, H., Lu, J., & Huang, Z. J. (2013). The Spatial and Temporal Origin of Chandelier Cells in Mouse Neocortex. *Science*, *339*(6115), 70-74. https://doi.org/10.1126/science.1227622

Tasic, B., Yao, Z., Graybuck, L. T., Smith, K. A., Nguyen, T. N., Bertagnolli, D., Goldy, J., Garren, E., Economo, M. N., Viswanathan, S., Penn, O., Bakken, T., Menon, V., Miller, J., Fong, O., Hirokawa, K. E., Lathia, K., Rimorin, C., Tieu, M., . . . Zeng, H. (2018). Shared and distinct transcriptomic cell types across neocortical areas. *Nature*, *563*(7729), 72-78. https://doi.org/10.1038/s41586-018-0654-5

Tosches, M. A. (2021). From Cell Types to an Integrated Understanding of Brain Evolution: The Case of the Cerebral Cortex. *Annu Rev Cell Dev Biol*, *37*, 495-517. https://doi.org/10.1146/annurev-cellbio-120319-112654

Tremblay, R., Lee, S., & Rudy, B. (2016). GABAergic Interneurons in the Neocortex: From Cellular Properties to Circuits. *Neuron*, *91*(2), 260-292. https://doi.org/10.1016/j.neuron.2016.06.033

Veres, J. M., Nagy, G. A., Vereczki, V. K., Andrási, T., & Hájos, N. (2014). Strategically Positioned Inhibitory Synapses of Axo-axonic Cells Potently Control Principal Neuron Spiking in the Basolateral Amygdala. *The Journal of Neuroscience*, *34*(49), 16194-16206. https://doi.org/10.1523/jneurosci.2232-14.2014

Viney, T. J., Lasztoczi, B., Katona, L., Crump, M. G., Tukker, J. J., Klausberger, T., & Somogyi, P. (2013). Network state-dependent inhibition of identified hippocampal CA3 axo-axonic cells in vivo. *Nature Neuroscience*, *16*(12), 1802-1811. https://doi.org/10.1038/nn.3550

Wang, B.-S., Bernardez Sarria, M. S., An, X., He, M., Alam, N. M., Prusky, G. T., Crair, M. C., & Huang, Z. J. (2021). Retinal and Callosal Activity-Dependent Chandelier Cell Elimination Shapes Binocularity in Primary Visual Cortex. *Neuron*, *109*(3), 502-515.e507. https://doi.org/10.1016/j.neuron.2020.11.004

Wang, X., Tucciarone, J., Jiang, S., Yin, F., Wang, B.-S., Wang, D., Jia, Y., Jia, X., Li, Y., Yang, T., Xu, Z., Akram, M. A., Wang, Y., Zeng, S., Ascoli, G. A., Mitra, P., Gong, H., Luo, Q., & Huang, Z. J. (2019). Genetic Single Neuron Anatomy Reveals Fine Granularity of Cortical Axo-Axonic Cells. *Cell Reports*, *26*(11), 3145-3159.e3145. https://doi.org/10.1016/j.celrep.2019.02.040

Zeppilli, S., Gurrola, A. O., Demetci, P., Brann, D. H., Attey, R., Zilkha, N., Kimchi, T., Datta, S. R., Singh, R., Tosches, M. A., Crombach, A., & Fleischmann, A. (2023). Mammalian olfactory cortex neurons retain molecular signatures of ancestral cell types. *bioRxiv*. https://doi.org/10.1101/2023.08.13.553130

Fig 1

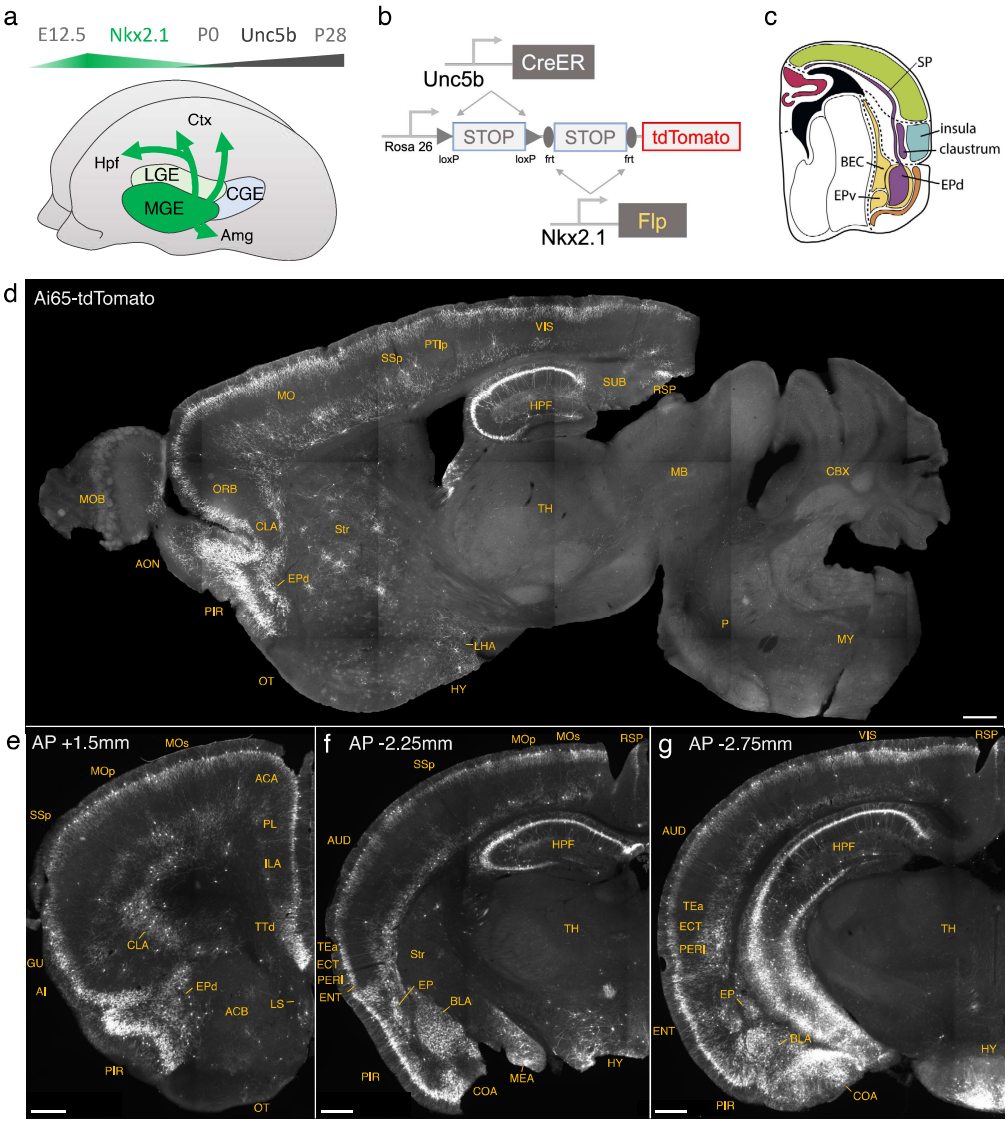

Fig 1 Suppl 1

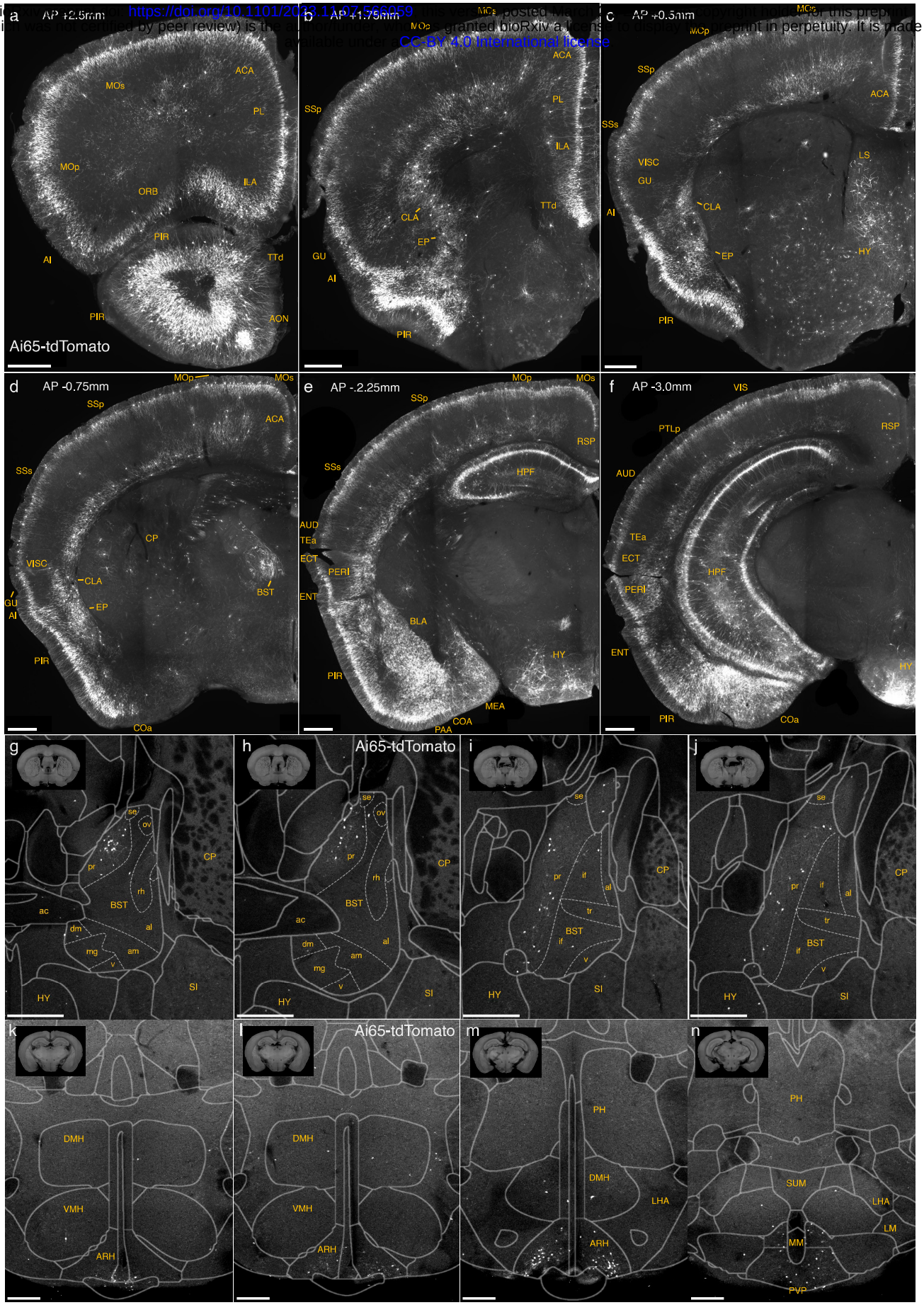

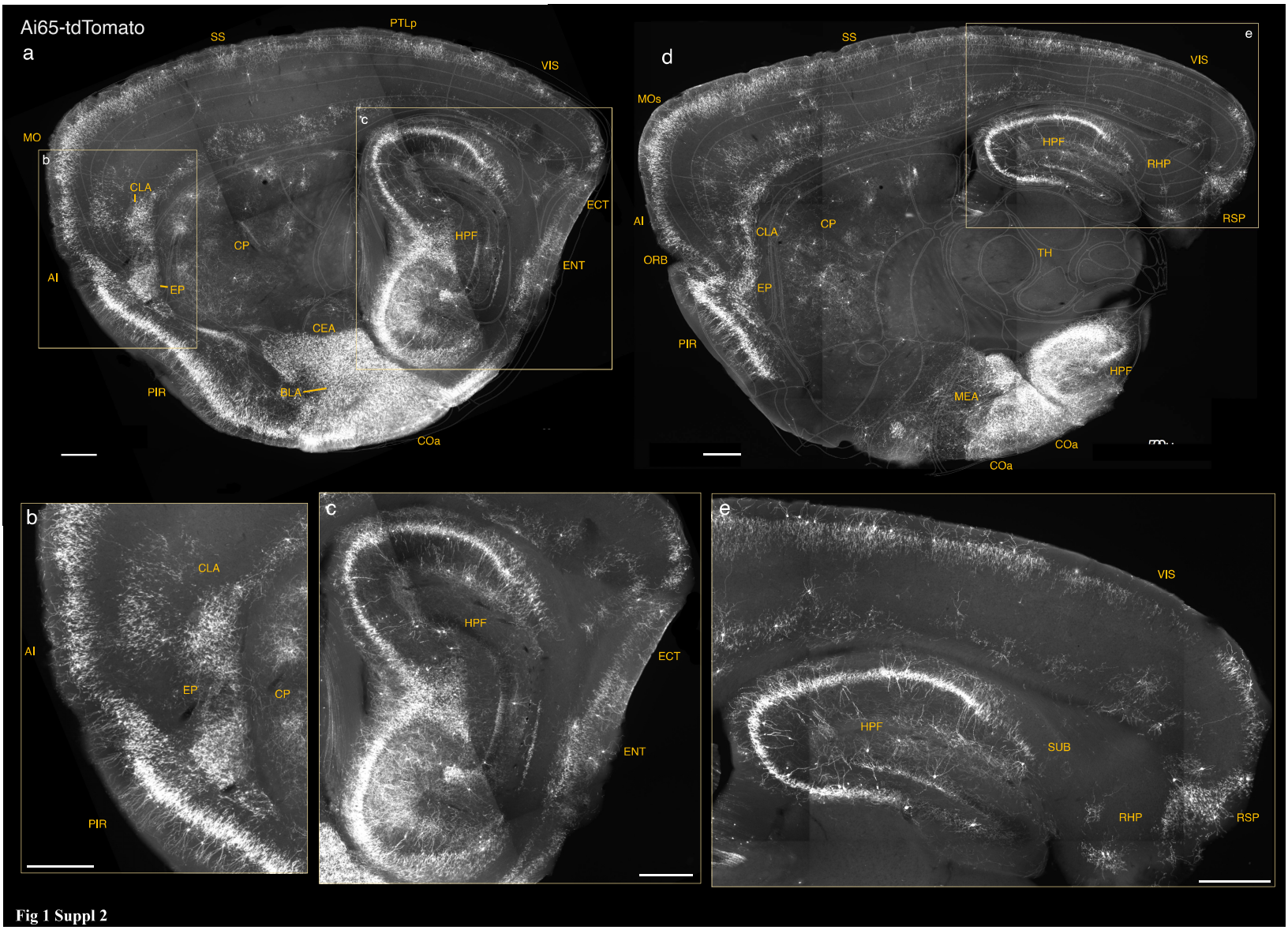

Fig 1 Suppl 2

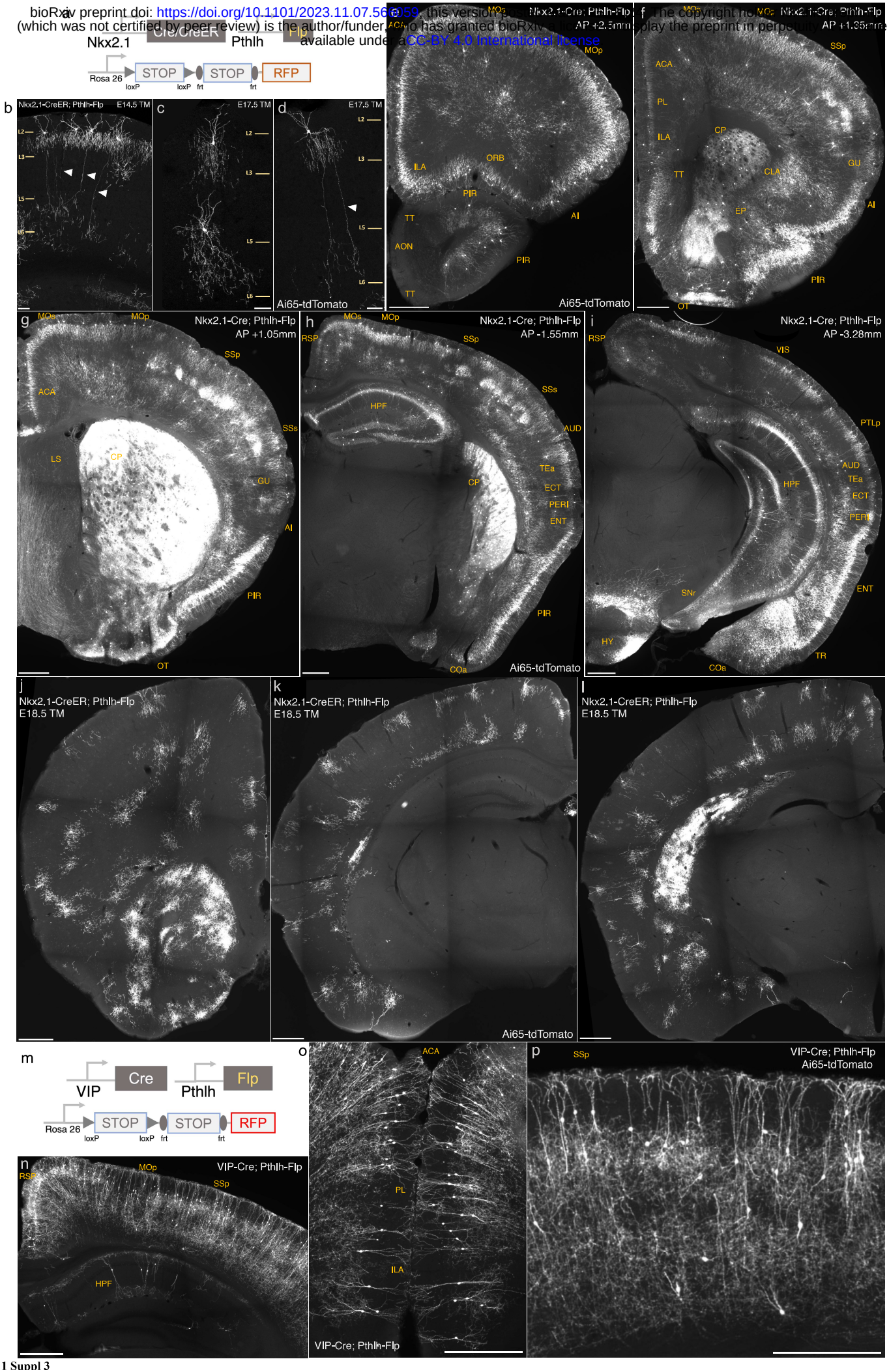

Fig 1 Suppl 3

Fig 2

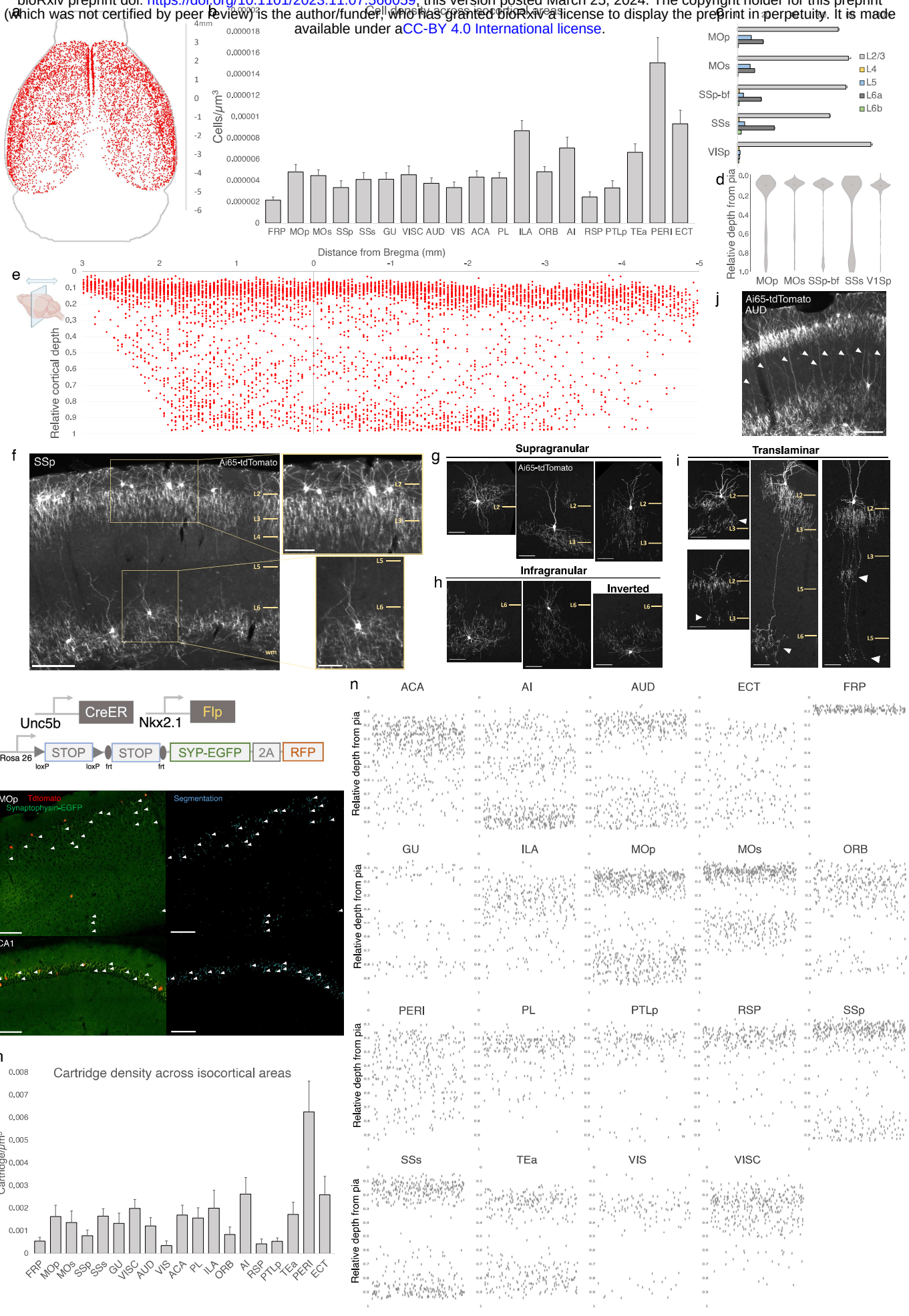

Fig 2 Suppl Fig 1

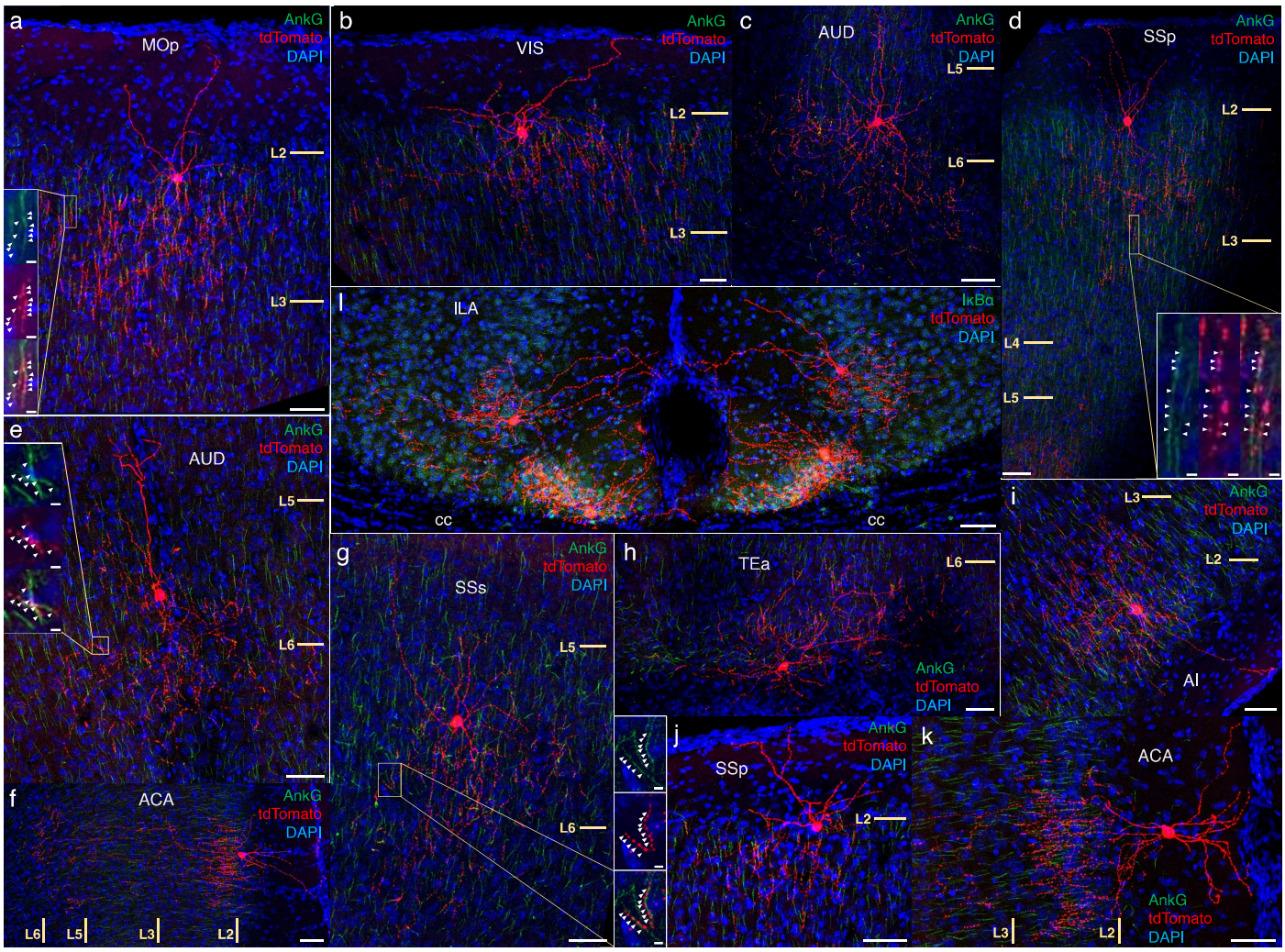

Fig 3

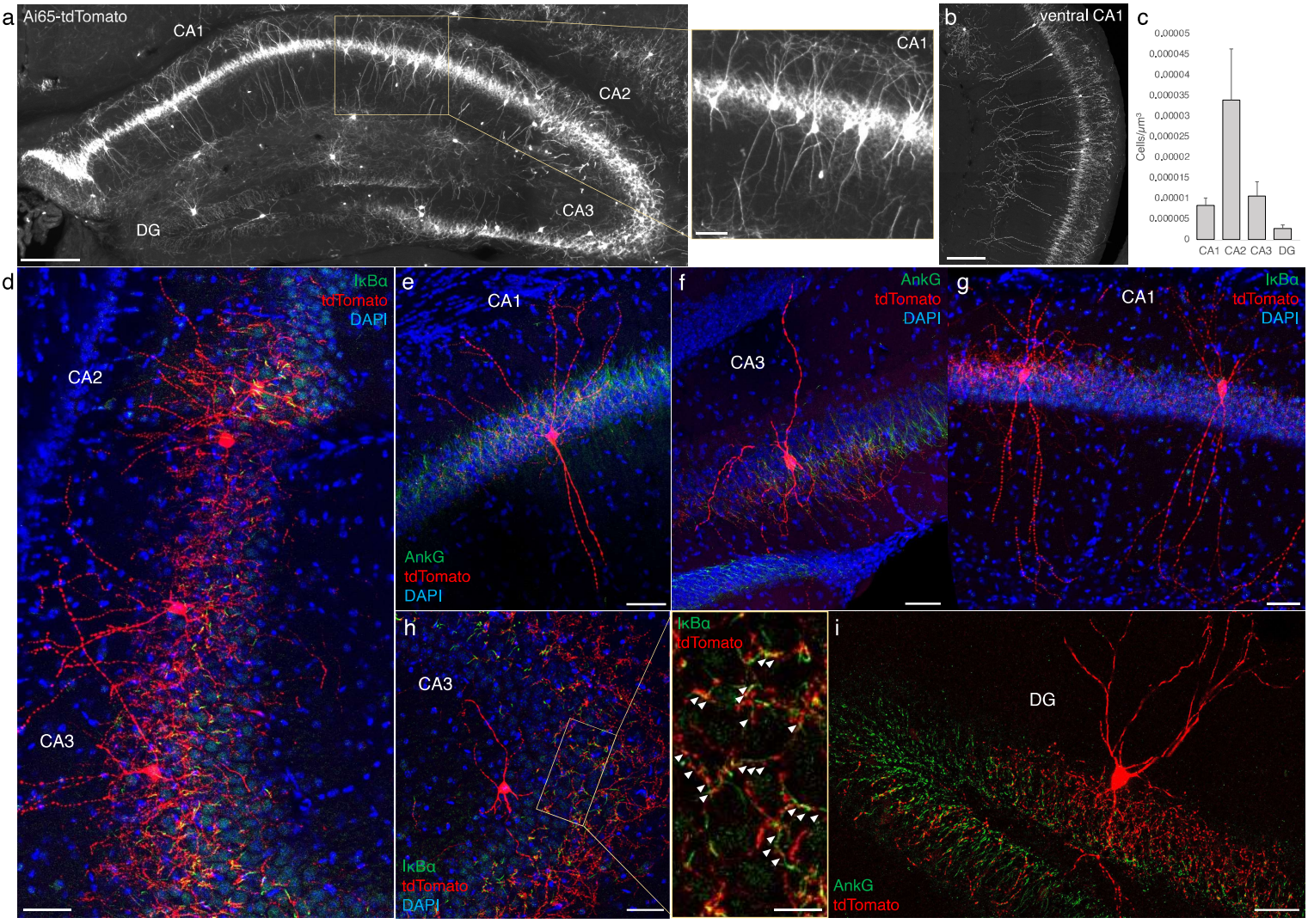

Fig 4

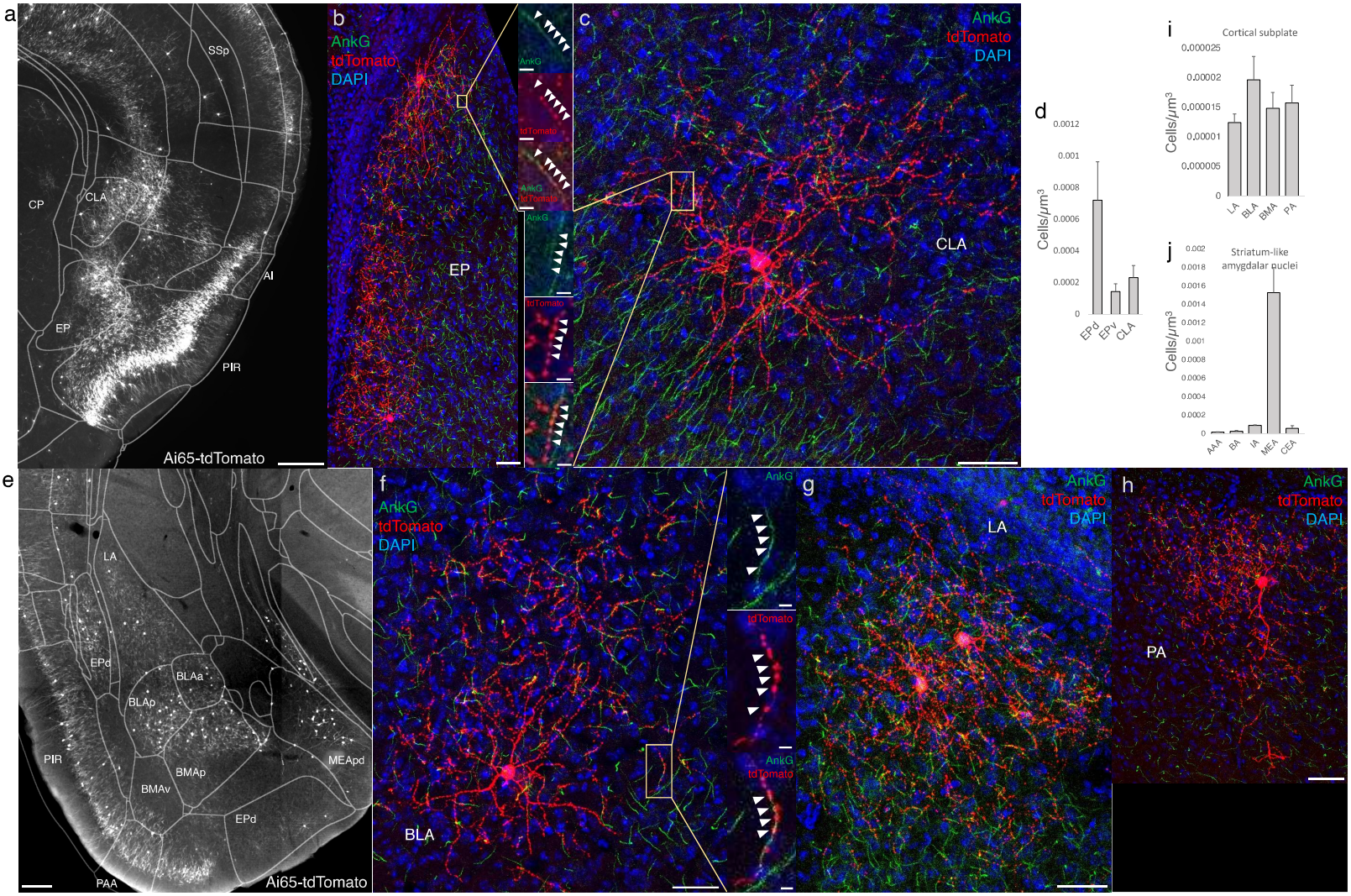

Fig 5

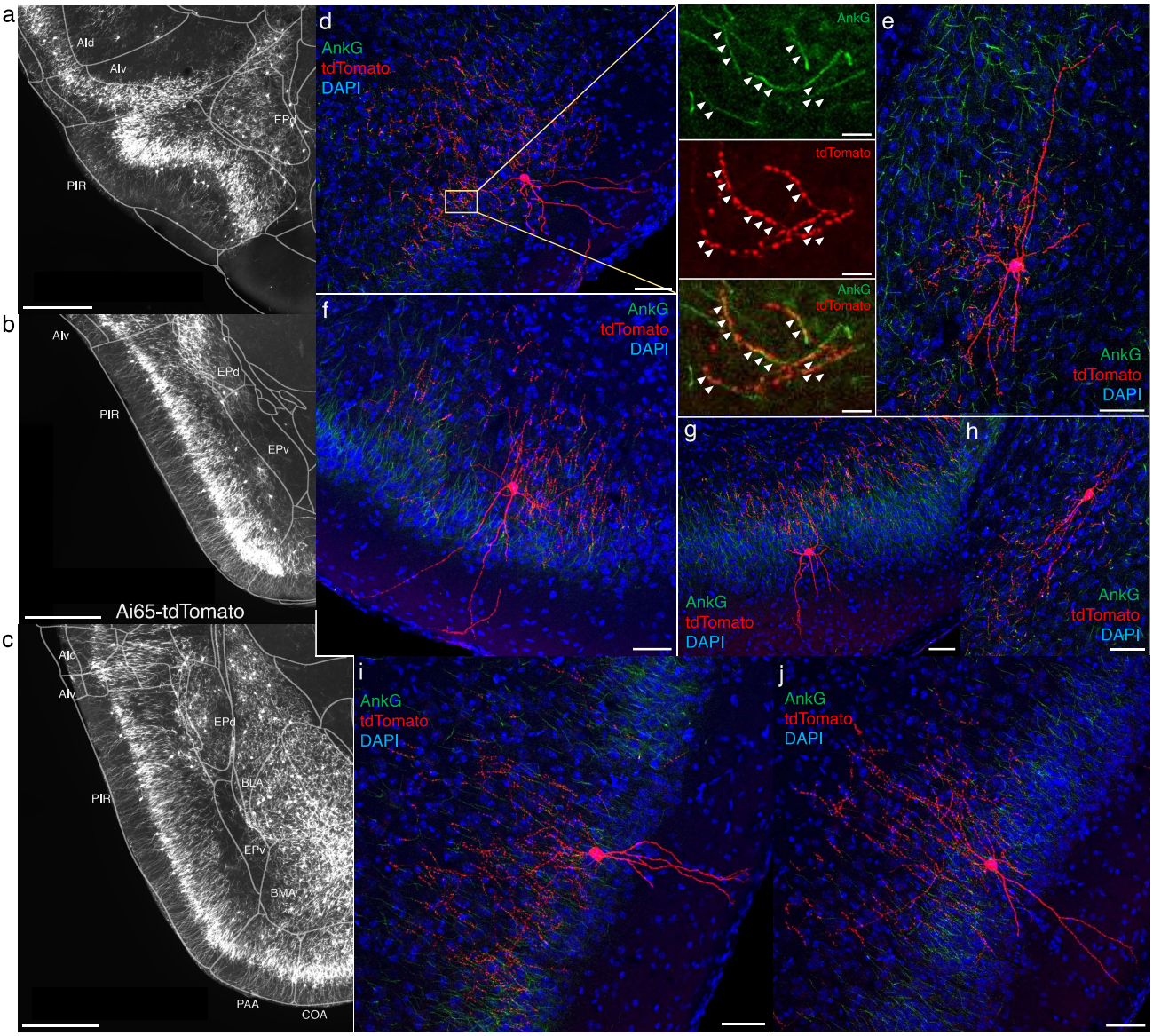

Fig 6

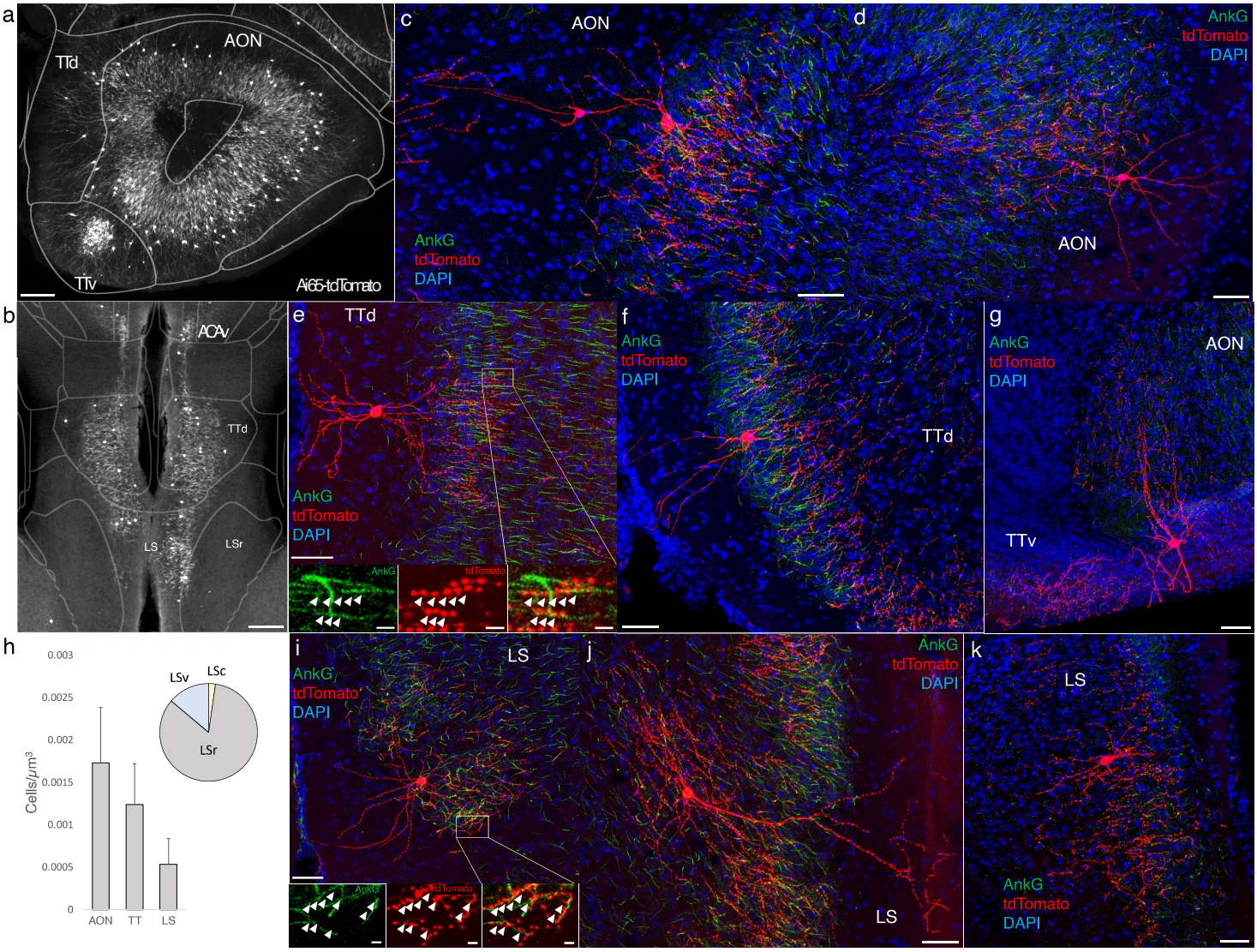

Fig 7

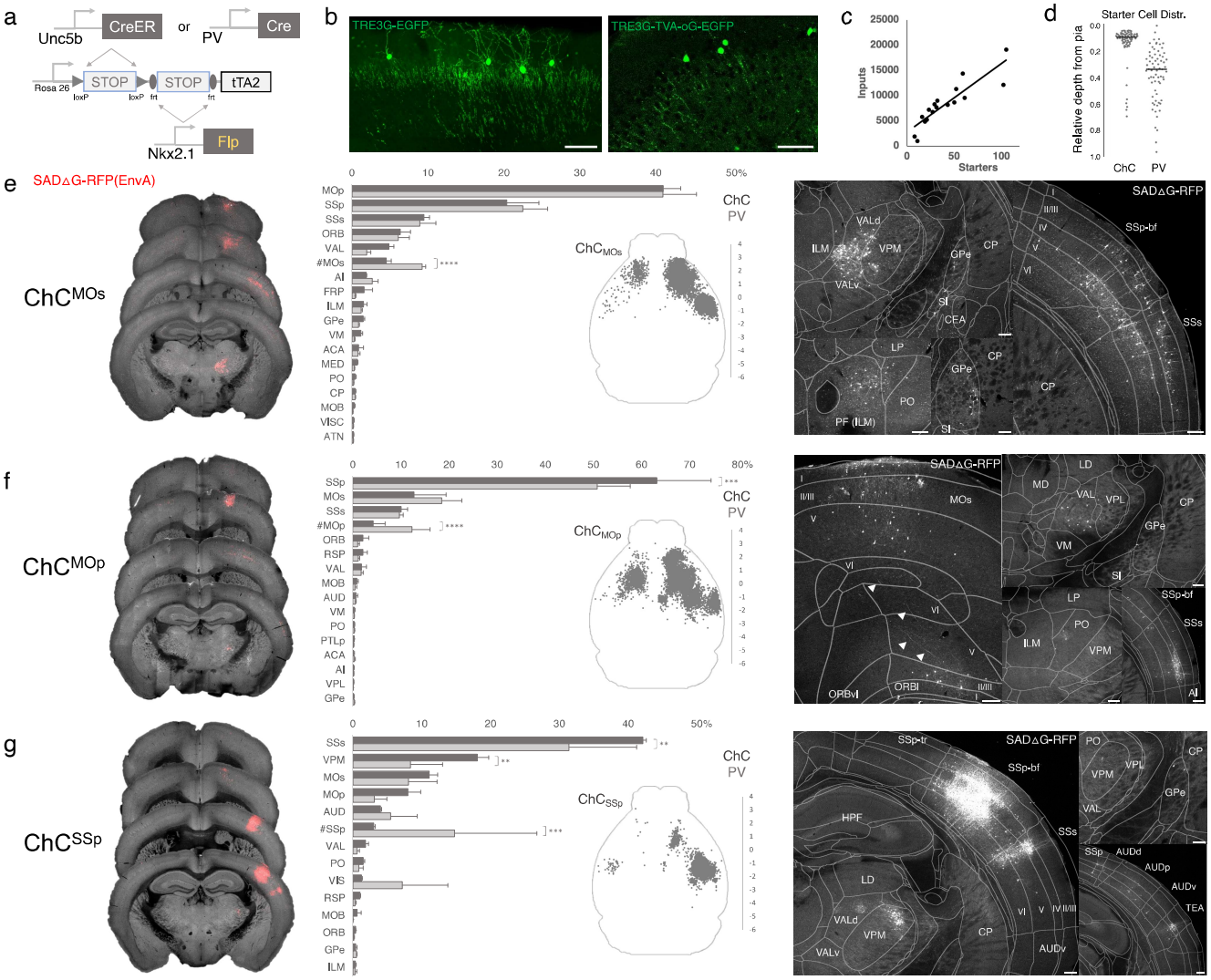

Fig 7 Suppl 1

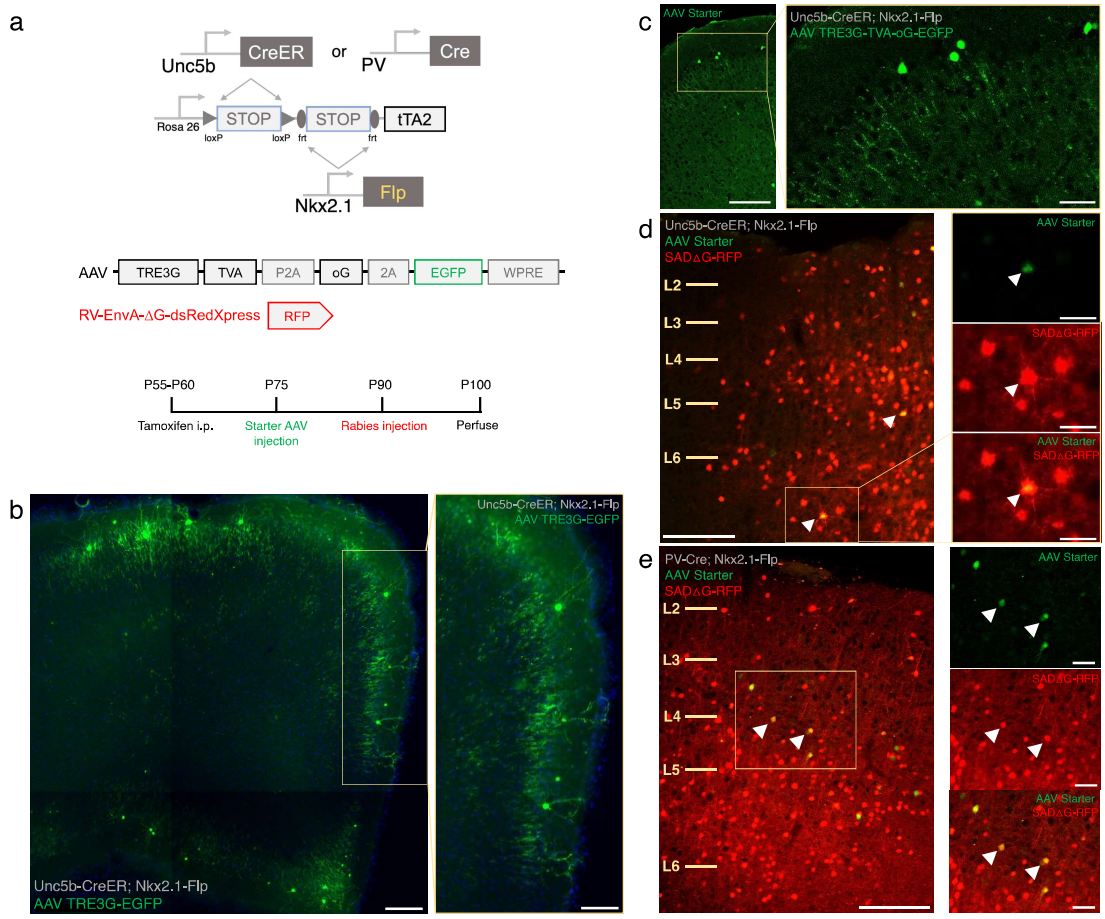

Fig 8

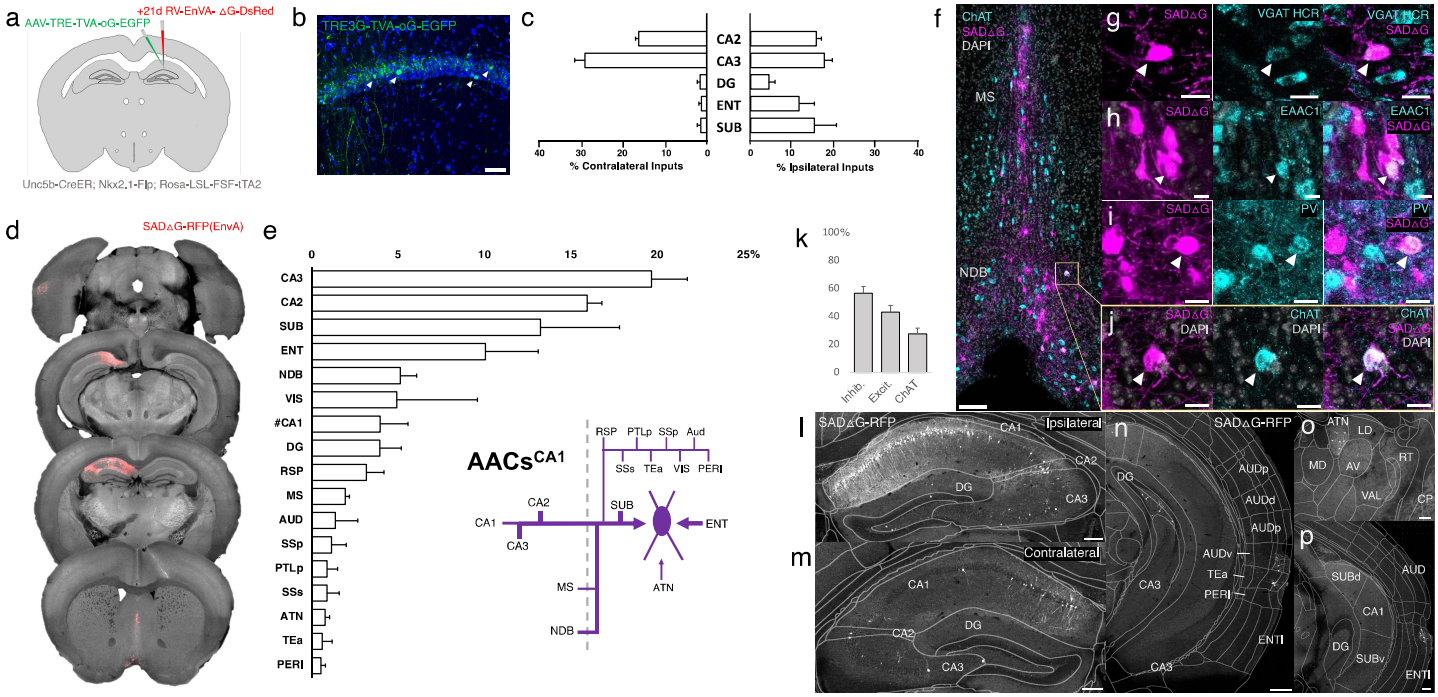

Fig 9

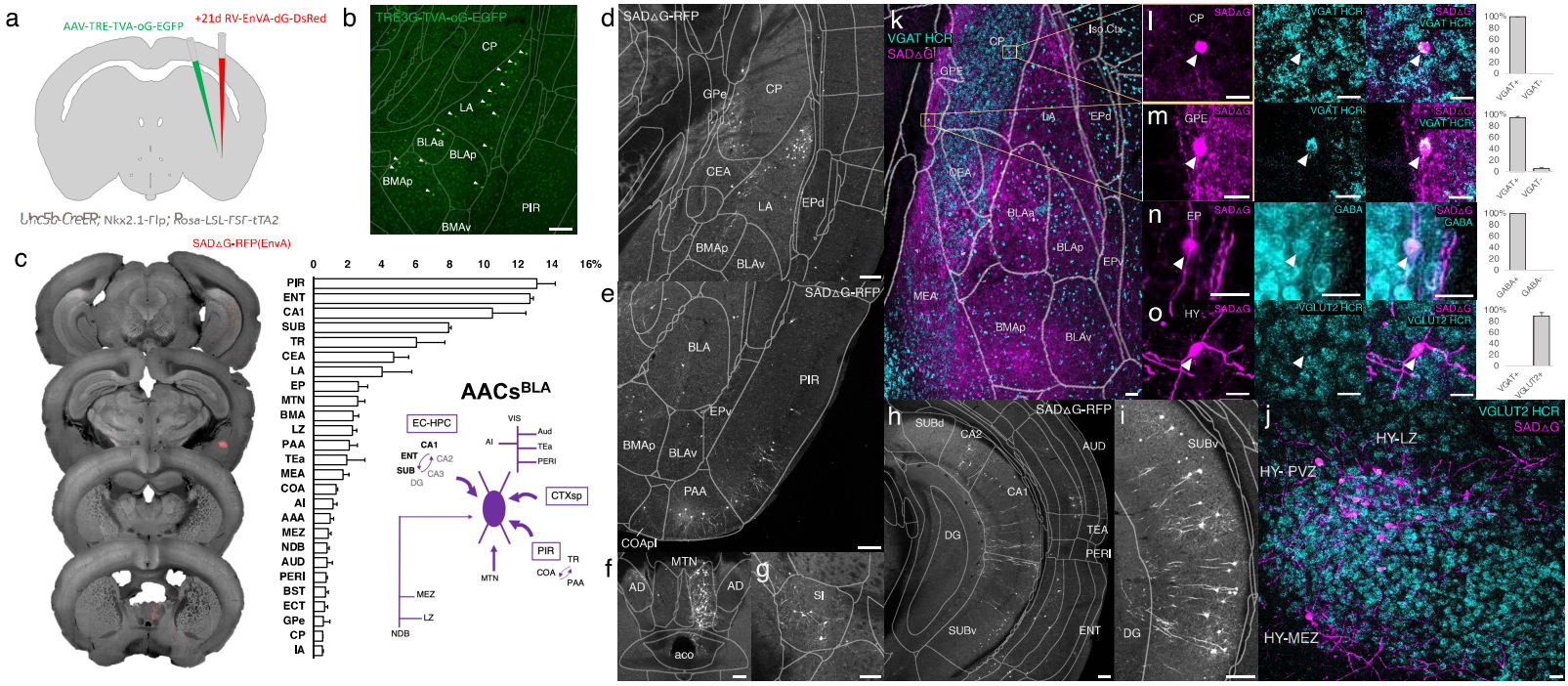

Table 1. Brain-wide distribution pattern of putative AACs

Developmental origin	Brain structure	Evolutionary term	Validation
Dorsal pallium	neocortex all cortical areas entorhinal, perirhinal	isocortex	yes
Medial pallium	hippocampal formation dentate, CA1, CA2, CA3 subiculum	archicortex	yes
Lateral pallium	claustrum insular endopirifom dorsal		not yet
Ventral pallium	amygdaloid complex - BLA - CoA - MEA - BMA extended amygdala - CeA (no AACs found) - BNST (putative cases only) olfactory cortex - piriform - endopiriform ventral [no]	paleocortex	yes
Septal neuroepithelium	-lateral and medial septum -tania tecta -AON		yes
Hypothalamo-telencephalic prosomere h1/h2	hypothalamus - arcuate nucleus - periventricular hypothalamic nucleus		not yet